Journal of Wind Engineering & Industrial Aerodynamics 206 (2020) 104224

Contents lists available at ScienceDirect

Journal of Wind Engineering & Industrial Aerodynamics

journal homepage: www.elsevier.com/locate/jweia

On the flow past and forces on double-stacked wagons within a freight train under cross-wind

Siavash Maleki, David Burton *, Mark C. Thompson

Fluids Laboratory for Aeronautical and Industrial Research (FLAIR), Department of Mechanical and Aerospace Engineering, PO Box 31, Monash University, 3800, Australia

ARTICLE INFO

Keywords:
Hybrid RANS/LES
Freight train
Train aerodynamics
Yaw
Cross-wind
Drag
Bluff-body flow

ABSTRACT

This paper analyses predictions from Large Eddy Simulations of a section of a double-stacked freight train subjected to various local loading configurations under the influence of cross-wind. In particular, drag, side force and moment coefficients of double-stacked containers on a test wagon were predicted for different combinations of upstream and downstream gaps between neighbouring wagons. The mean flow field around a loaded test wagon was shown to undergo a significant topological change with increasing gap size and yaw angle. The gap range where the drag increases most rapidly was found to change as yaw angle is increased. Various topological changes to the flow over the vehicle were identified using the mean and fluctuating pressure coefficients, and a Proper Orthogonal Decomposition analysis, revealing the dominant flow mechanisms over the roof and at the leeward side of the vehicle, due to the unsteadiness in the flow over those regions. In addition to the fluctuating and extreme aerodynamic side force, the development of mean wake structure with increasing yaw angle are discussed.

1. Introduction

The study of freight train aerodynamics is motivated by potential improvements in fuel economy and reductions in greenhouse gas emissions. At typical cruising speeds, approximately 80% of overall drag experienced by a freight train is due to air resistance (Raghunathan et al., 2002). However, in addition to the economic reasons and environmental concerns, the aerodynamic stability of freight trains is of great importance. Freight trains cruising in a strong cross-wind are at high risk of overturning or derailment as the empty containers could be blown off. For example, a famous freight train side-wind accident occurred on March 2008 in the UK where five empty containers were blown off the train (RAIB, 2008).

The task of formulating a general methodology for approximating the aerodynamic forces on a freight train has been an ongoing challenge. This is due to the endless possible loading patterns of any train, resulting in widely varying aerodynamics. Indeed, the variety of different sized shipping container types can lead to a seemingly infinite number of ways of loading a freight train. In addition to this, the position of containers within a train can vary over a trip due to removal of existing containers or introduction of new ones at intermediate loading hubs. Furthermore, the containers can be loaded single- or double-stacked; the latter is of particular interest to the present study, doubling the standard height-to-width ratio.

Apart from their variation in geometry, the great challenge in modelling the aerodynamics of freight trains, both numerically and experimentally, is their extreme lengths that can reach up to ~2 km, corresponding to a length-to-height ratio of $L/H = 250–500$. Modelling a full-length train in a wind-tunnel necessarily requires a massive reduction in scale, and beyond that moving ground planes have limited lengths. Even with a moving floor, on such a small-scale model, the ratio of the floor boundary-layer thickness to train height becomes unacceptably high and the reduced Reynolds number would lead to reduced reliability of predictions of the aerodynamics of a real full-scale train.

Various authors ((Engdahl et al., 1986a; Engdahl et al., 1986b; Watkins et al., 1992; Golovanevskiy et al., 2012)) conducted studies to determine the effects of wagon position within a train on the aerodynamic drag, using models with different numbers of wagons included. The general consensus appears to be that after the first one or two wagons the drag on a wagon stabilizes to a near constant value. The exception appears to be the study of (Gielow and Furlong, 1988) who found drag stabilization occurs beyond the eighth wagon.

Li et al. (2017) adopted a similar approach to the above studies to look at the general case where the gaps between wagons were varied.

* Corresponding author.
E-mail address: david.burton@monash.edu (D. Burton).

https://doi.org/10.1016/j.jweia.2020.104224
Received 4 November 2019; Received in revised form 7 April 2020; Accepted 1 May 2020
Available online 26 August 2020

Their setup consisted of seven wagons aligned longitudinally, where the test (instrumented) wagon was placed between the three upstream and downstream wagons, in an attempt to model a wagon at an arbitrary position in a freight train. The localised aerodynamic drag of the test wagon was determined for 7 different upstream and downstream gap sizes (G_{front}, G_{base}), resulting in a combination of 49 gap size combinations. Their findings showed increasing drag for increasing gap sizes, but with the drag experienced for the test wagon increasing more rapidly in the range $1.77W - 3.23W$ (W = wagon width).

As a result of having a significant length-to-width ratio, side forces induced by cross-winds are an important consideration. When the oncoming flow is directed longitudinally towards the back of a train, only the (longitudinal) forces normal to the front and rear surfaces of the container affect the aerodynamic drag. However, when it is angled relative to the longitudinal axis of a train, there is mean crossflow through the inter-wagon gaps that can contribute to the aerodynamic drag. Specifically, cross-winds promote flow separation on the upper side of sharp edges of the container promoting streamwise vortices, change the boundary-layer development along the train, and alter the flow in the inter-wagon gaps, all affecting the aerodynamic drag of transported containers.

Engdahl et al. (1986b), Gielow and Furlong (1988), and Golovanevskiy et al. (2012) reported the forces applied to a container within a train subjected to a minimum inter-wagon gap size up to 20° yaw angle. They showed a consistent increase in drag with respect to cross-wind angle. An attempt was made by Watkins and Saunders (Watkins et al., 1992) to obtain the drag variation as a function of inter-wagon gap size and cross-wind angle. In their wind-tunnel experiment, four inter-wagon gap sizes up to 15° yaw angle in increments of 3° were tested. No noticeable increase in drag was reported as the inter-wagon gap spacing was increased from 0.55 to 0.83 m for yaw angles below 12°. However, the drag penalty became significant for the higher gap sizes of 1.27 and 1.87 m for all yaw angles tested.

Soper et al. (2015) carried out moving-model cross-wind experiments at only a yaw angle of 30° to assess the influence of the container loading configuration and the presence of the gap upstream and downstream of a container on the aerodynamic coefficients. They reported that a decreased loading efficiency and the existence of an upstream gap increases the aerodynamic forces and hence the risk of overturning. In related studies, Flynn et al., 2014, 2016 used large eddy simulations to look at the effect of crosswinds, but mainly focused on the effects on slipstream.

Recently, the effect of loading configuration on a 1/20th scaled-down model of a freight train under cross-wind was investigated by Giappino et al. (2018). Their experimental model consisted of a front engine and two instrumented freight carriages, which enabled them to test eight various loading configurations for yaw angles from 0 to 90°. Despite an insufficient number of wagons being used to model an arbitrary section of a train, their findings showed that the smallest drag occurs when all containers are placed on the flat cars at the smallest gap spacing, acting like a single body, while the greatest drag penalty was observed with the removal of the upstream container. For the configuration in which the wagon was placed at the last position and its upstream wagon is removed, the drag was found to increase sharply up to 25° yaw angle, after which it reduced until it reached a value close to zero for 90° yaw angle.

In conclusion, previous investigations have tended not to consider the effect of loading configurations of upstream and downstream wagons on flow around a loaded wagon under cross-wind conditions, which is a key aim of the current study. Additionally, little information has been provided in past studies regarding the details of the flow fields associated with the various loading configurations under cross-wind.

Thus, the main objectives of this paper are to: (i) obtain estimates of the aerodynamic drag, side force and moment coefficients experienced by a double-stacked container in the middle section of a freight train subjected to different local loading configurations in cross-wind; and (ii) to identify and determine the influence of the dominant flow structures and characteristics of the flow around a double-stacked container as a function of loading configuration and cross-wind, which are in turn connected to the recorded aerodynamic force variations.

The main reason for performing cross-wind simulations of this setup is the difficulty associated with modelling more than slightly yawed configurations experimentally. This is because a wind-tunnel with a very large cross section and long test section would be required to ensure the blockage ratio remains below 10%, in agreement with the requirements of European Rail Agency (European Rail Agency, 2008). Additionally, numerical investigation allows the flows inside the different-sized upstream and downstream gaps, and the flow around the wagon to be characterised as yaw angle increases, while the velocity field could not be measured using available techniques (Cobra probes) due to device limitations.

It should be noted that the present investigation follows on from the results of zero-yaw simulations conducted by Maleki et al. (2019), in which a similar setup to that of Li et al. (2017) was modelled. The key goals of that study were to model the change in the flow over the critical front gap range of $1.77W - 3.23W$ and to understand the underlying flow mechanisms responsible for that high rate of drag increase.

The yaw angle (ψ) seen by a wagon is defined as the angle between the wagon centreline and the mean direction of the wind as seen by the moving wagon. As the primary motivation for this work is aerodynamic drag under different environmental conditions, several loading configurations were considered for more usual small to moderate yaw angles of 0° to 20°, and only the two most extreme cases were examined for higher yaw angles of $\geq 30°$. This is because, a train travelling at 110 km/h will experience a yaw angle less than 20° more than 94% of the time, based on a Rayleigh probability distribution for a mean environmental wind speed of 25 km/h.

The paper is structured as follows. Initially, the simplified freight wagon geometry, the computational domain and boundary conditions, and simulation methodology and analysis methods are discussed. Following this, the validated methodology is applied to predict the flow past and forces on a representative section of a model freight train as the flow is increasingly yawed. The behaviour is analysed in terms of changes to the flow topology relative to the non-yawed reference cases. Finally, the paper ends with conclusions to connect the results with double-stacked freight trains subject to different loading configurations.

2. Methodology

2.1. Model description

The numerical model employed in this study represents a section of a highly simplified freight train model subjected to various local loading configurations and yaw angles. This model is based on the multi double-stacked container setup that was tested by Li et al. (2017) in a 450 kW closed-circuit wind tunnel at Monash University in a parallel experimental research program.

The experimental setup was developed based on the assumption that the combined aerodynamic force experienced by the entire freight train can be modelled as a summation of contributions from individual wagons. This approach was considered by Li et al. (2017) who determined the localised effects of differently loaded wagons that could be used to construct such an overall drag estimate. An arbitrary wagon's aerodynamic characteristics are then a function of its upstream flow conditions, and its downstream blockage, which in turn is a function of the loading configurations surrounding that wagon.

The geometry used for our numerical investigations is a 1:14.6 scale model of 14.6 m long double-stacked container wagon, similar to that used for experimental tests by Li et al. (2017). The overall model dimensions are $L = 1000$ mm, $W = 171$ mm and $H = 438$ mm, nominally representing a wagon at a nominally arbitrary position along of a freight train. The ground clearance was $E = 28$ mm, corresponding to a standard wheel size. In line with the experimental model, the additional

geometrical features of real wagons, such as underbody bogies and panel ribbing, were omitted, simplifying the wagon to a rectangular prism. These dimensions were based on a commonly sized double-stacked container, which is the dominant-sized container shipped around Australia.

To model an arbitrary section of a freight train, seven double-stacked container wagons were aligned longitudinally: three initial wagons followed by a test wagon and then three trailing wagons. All wagons had identical geometry excluding the leading wagon, which had a rounded nose, similar to that of an Ahmed body (Ahmed, 1983), to limit front-edge flow separation. The spaces between upstream and downstream wagons, apart from those immediate to the test wagon, were covered to focus on the local loading configuration, consistent with the matching zero-yaw experiments. Note that no discernible change in pressure drag coefficient (C_{Dp}) was found when the spaces between the upstream and downstream wagons were tested covered and uncovered for the four different loading configurations experimentally. A fuller description of the experimental setup is given in (Li et al., 2017).

In addition to these simplifications, the influence of floor boundary-layer thickness and relative motion between the train and the ground were not considered in this study. However, it is worth pointing out that the boundary layer displacement and momentum distances were measured as $0.036H$ and $0.031H$, i.e., 3–4% of train height, at the position of the test wagon, as measured by Li et al. (2017) in the parallel experimental program. This suggests that the effects of choosing a stationary rather than a moving ground are likely to be relatively small.

Moreover, all wagons were *double-stacked*; single-stacked wagons were not considered. Overall, the reason for omitting these details was primarily to reduce model complexity, allowing an initial focus on the effect of the upstream and downstream gap size combinations on the flow in the vicinity of the test wagon without extraneous factors affecting the results. Of course, the inclusion of these additional features could have a non-negligible effect on the flow, and it would be advantageous to include at least some of them in future studies.

2.2. Computational domain and boundary conditions

The freight train is positioned in a hexahedral computational domain. The top and side views of the computational domain and the coordinate system used herein can be seen in Fig. 1. The height of the computational domain was fixed for all simulations, while its lateral dimension was increased with increasing yaw angle to ensure the maximum blockage ratio in this study remained below 2.5%. As an example, the lateral dimension of computational domain at 20° yaw angle is depicted in Fig. 1(a). The origin of the computational domain coordinate system is the centre of the lower edge of the test wagon front surface.

For all simulations, the top and side of the computational domain were set to a zero-shear wall condition. A no-slip boundary condition was applied to the ground surface of the domain (also matching the wind-tunnel experiments). The outlet of the computational domain was set as a constant pressure outlet located three wagons downstream of the test wagon. This distance is assumed to be sufficient to induce the minimal upstream effects on the flow in the regions of interest.

The yaw angles simulated in this study were 0°, 5°, 10°, 20°, 30°, 45° and 90°. The range of gap sizes selected in this investigation was from $0.3W$ to $6.46W$ since $0.3W$ is the smallest (standard) inter-wagon gap size and $6.46W$ is equivalent to a single empty container-wagon. For yaw angles $\leq 20°$, both upstream (G_{front}) and downstream gap (G_{base}) sizes were progressively varied to cover the range $0.3W \leq G_{front,base} \leq 6.46W$, while the opposite gap was kept constant at $0.3W$. Additionally, the gap combination $G_{front} = 6.46W$ and $G_{base} = 6.46W$ was simulated to study the influence of varying both upstream and downstream gaps together. The seven gap combinations simulated for yaw angle $\leq 20°$ were: $G_{front} = 0.3W$, $1.77W$, $3.23W$ and $6.46W$ at constant $G_{base} = 0.3W$; $G_{base} = 3.23W$ and $6.46W$ at constant $G_{front} = 0.3W$; $G_{front} = 6.46W$ and $G_{base} = 6.46W$. For yaw angles $\geq 30°$, only the two most extreme cases for $G_{front} = 0.3W$ and $6.46W$ at constant $G_{base} = 0.3W$ were examined. Hence, the overall number of IDDES (Improved Delayed Detached Eddy Simulation - discussed in Section. 2.4) computations performed was 34, and these are listed in Table 1.

As mentioned above, the experimental setup developed by Li et al. (2017) consisted of seven wagons in tandem, where the test wagon was located at the 4th position. However, in the present study, the number of upstream wagons was reduced to 1.5 (for 0° yaw angle) and 2.5 wagons (yaw angle of $\geq 5°$ up to 45°) to constrain the computational mesh size and hence cost, while the number of downstream wagons was kept at 3.

For 0° yaw angle, the inlet of the computational domain was placed at the middle of the second wagon, due to the availability of the experi-

Table 1
List of loading configurations and yaw angles simulated in this study.

Yaw = 0°, 5°, 10° and 20°:	Yaw = 30°, 45° and 90°:
$G_{front} = 0.3W$ and $G_{base} = 0.3W$	$G_{front} = 0.3W$ and $G_{base} = 0.3W$
$G_{front} = 1.77W$ and $G_{base} = 0.3W$	$G_{front} = 6.46W$ and $G_{base} = 0.3W$
$G_{front} = 3.23W$ and $G_{base} = 0.3W$	
$G_{front} = 6.46W$ and $G_{base} = 0.3W$	
$G_{front} = 0.3W$ and $G_{base} = 3.23W$	
$G_{front} = 0.3W$ and $G_{base} = 6.46W$	
$G_{front} = 6.46W$ and $G_{base} = 6.46W$	

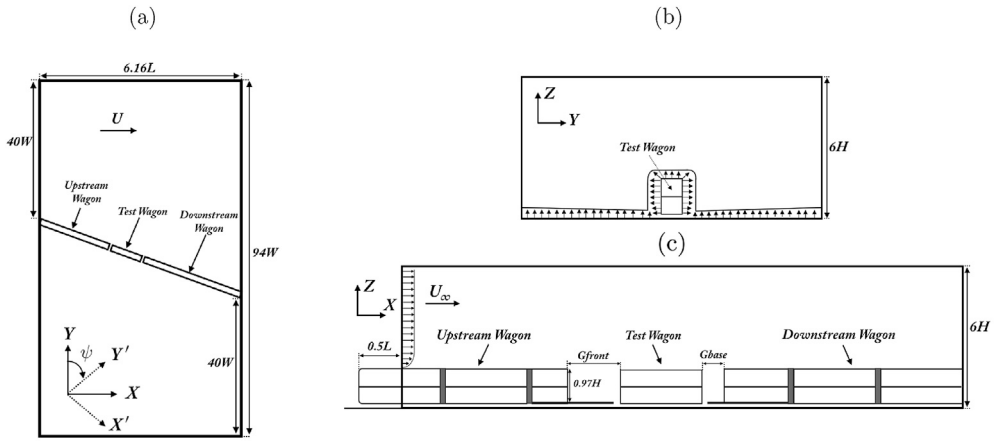

Fig. 1. Schematics of the multiple double-stacked wagons yawed within the computational domain, showing a front and base gaps. (a) Top view for gap ratio combination $G_{front} = 0.3W$ and $G_{base} = 0.3W$ at $\psi = 20°$ (Not to scale). (b) Normal view at zero yaw angle, showing the boundary layer around the upstream wagon, where the velocity profile is recorded. (c) Side view for $\psi \geq 5°$ up to 45°, where the inlet is placed at the middle of first wagon.

mental boundary-layer profile measured at that position. For yaw angles $\geq 5^{\circ}$ up to 45°, the inlet was located at the middle of the first wagon (see Fig. 1b). The inlet condition of these simulations was obtained from another simulation based on the steady RANS (Reynolds Averaged Navier-Stokes) *SST* (Shear Stress Transport) model. In those time-mean simulations, the multiple wagons setup, in which three wagons were placed upstream and downstream of the test wagon, was yawed, and the velocity around the middle of the first wagon and near the ground were recorded. These velocity profiles were used as the inlet condition for the IDDES simulations for each corresponding yaw angle. The inlet for all RANS *SST* simulations was placed 4.23 m upstream of the front surface of the test wagon, equivalent to the leading edge of the splitter plate used in the wind-tunnel experiment (Li et al., 2017) to reduce the effect of the ground boundary-layer. The inlet condition for these RANS *SST* simulations matched the flow profile measured at that location in the wind-tunnel experiment. The velocity profile at the inlet had a 30 ms^{-1} free-stream velocity, U_{∞}, corresponding to a Reynolds number based on wagon width of $Re_w = 0.3 \times 10^6$, again matching the zero-yaw experiments. This effectively meant that the train speed was reduced with yaw as the resultant apparent wind speed was kept constant for all the yaw angles. For a yaw angle of 90°, the multiple-wagons setup was yawed 90° and located 4.23 m downstream of the inlet that used inlet conditions from RANS *SST* simulations.

Note that the reason behind rotating the multiple-wagons setup with respect to the inlet as opposed to the simpler approach of changing the direction of the inlet velocity was that the results for zero-yaw simulations herein and also in Maleki et al. (2019) were based on the inlet condition matching the flow profile measured at the leading edge of the splitter plate used in the wind-tunnel experiment (not a constant velocity at inlet). Hence, the only way to follow on from the zero-yaw inlet condition and accurately model the flow condition under cross-wind and to match the experimental setup was to rotate the multiple-wagon setup with respect to the inlet. In other words, for the RANS *SST* simulations greater than zero yaw angle, had the multiple-wagons setup not been rotated, only a constant inlet velocity could have been used. This would have effectively resulted in a different inlet condition compared to zero-yaw experiments/simulations.

2.3. Meshing strategy

The Cartesian cut-cell approach was employed to generate the meshes for the IDDES simulations, as illustrated in Fig. 2. This meshing strategy allows significantly higher grid resolution around the wagons and inside $G_{front,base}$ with a relatively smooth but stepped transition to lower concentration away from the wagons.

An example of the mesh refinement regions when the multiple-wagons setup is yawed at 20° yaw angle can be seen Fig. 2. Of course, similar refinement regions and meshing parameters were used for constructing all grids, except the lateral size of Refinement B. This was increased with increasing yaw angle to ensure the vortical structures forming from flow separation from the upstream/downstream wagons are retained within this refinement region.

The number of *inflation layers* (i.e., compressed near-wall cell layers) used to capture the near-wall boundary layers were kept at 20 for all simulations. For the cells closest to the no-slip boundaries, the y^+ variation on the test wagon is reported in Table .2 only for the gap combination $G_{front} = 6.46W$ and $G_{base} = 6.46W$, and for $\psi = 10^{\circ}$, to give an indication of near-wall grid resolution.

While this near-wall resolution is insufficient to resolve fine-scale near-wall boundary-layer structures, it is consistent with modelling the larger length-scale separated flow from fixed separation points and subsequent wake development in an LES context. The typical numbers of cells contained within different meshes are presented in Table .3.

2.4. Numerical method

The commercial flow-simulation package ANSYS FLUENT version 16.1 was used for the simulations. The simulations in this study used the Improved-Delayed Detached Eddy Simulation (IDDES) turbulence model. The IDDES model incorporates the *Wall-Modelled* LES (Large Eddy Simulation) (WMLES) and *Delayed Detached Eddy Simulation* (DDES) models.

Detached Eddy Simulation (DES), which the DDES model is based on, is a hybrid approach proposed by Spalart et al., 1997 that employs a RANS model to capture the mean boundary-layer behaviour and LES to resolve the large eddies further away from the boundaries. The original DES formulation had a number of deficiencies to do with switching between the RANS and LES models near boundaries. This led to the

Table 2
The y^+ variation on the test wagon subjected to $G_{front} = 6.46W$ and $G_{base} = 6.46W$ at 10° yaw angle.

Surface	Range of y^+	Average
Front	0.4–4.5	2.3
Base	0.2–2.8	0.9
Windward side	1.3–4.0	2.4
Leeward side	0.5–3.7	1.9
Top	0.5–3.4	2.4

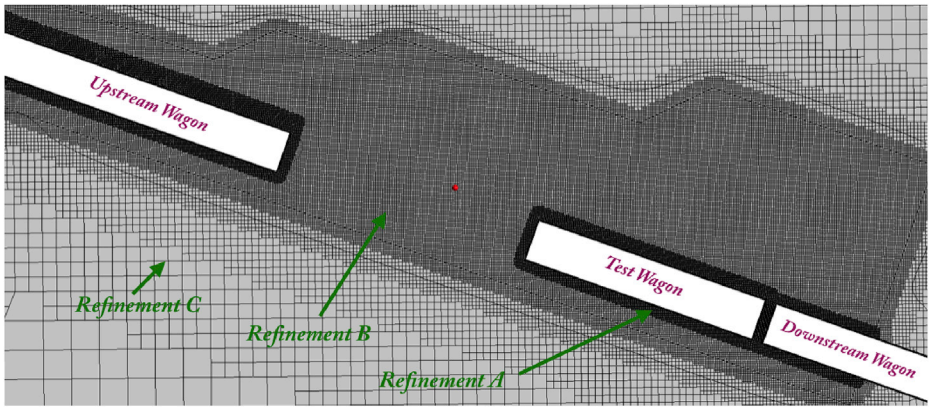

Fig. 2. A visualisation of mesh refinement around the wagons in the *x-y* plane at $z/H = 0.5$ for gap ratio combination $G_{front} = 6.46W$ and $G_{base} = 0.3W$, and for at $\psi = 20^{\circ}$. The positions of the upstream and downstream wagons as well as the test wagon are shown for this gap combination. Please refer to Table 3 for the cell size used in the refinement A, B and C for all grids.

Table 3
Meshing parameters for gap ratio combination $G_{front} = 0.3W$ and $G_{base} = 3.23W$ at 10° yaw angle.

Mesh	Coarse	Fine
Cell size wagon surface (Refinement A)	0.008m	0.004m
Cell size wake (Refinement B)	0.016m	0.008m
Cell size far-field (Refinement C)	0.06m	0.03m
No. of inflation layers	10	20
Wagon surface wall y^+	4–40	0.2–4
No. of cells (millions)	2.8	15

development of the DDES model to treat this problem. In turn, the DDES model was later improved by Shur et al. (2008) through combining the DDES and WMLES capabilities, referred to as *Improved-Delayed* DES (IDDES). The *wall-model* of WMLES enables more accurate capturing of the near-wall boundary-layer behaviour if there is sufficient grid resolution. A full description of the IDDES model can be found in Spalart (2009).

A (time-dependent) turbulence intensity of 1% was applied at the inlet, in line with wind-tunnel experiments. To account for the temporally and spatially varying characteristics of turbulence at the inlet, *synthetic turbulence* was added to the mean velocity profile based on a collection of point vortices. The approach, called the *Vortex Method* (VM) in ANSYS, generally bases the properties of the vortices on an upstream RANS simulation. This enables time-dependent turbulent fluctuations to be added to the zonal inlet flow to mimic background turbulence in an approximate sense (Mathey et al., 2006). This approach has been successfully used to treat aerodynamics of a train in (García et al., 2015).

Different timesteps were used in this study, as it was necessary to reduce the timestep with increasing yaw angle to ensure the Courant number remained below unity for the smallest cells. The minimum and maximum timesteps used were $0.003T_{\mathrm{ref}}$ and $0.00075T_{\mathrm{ref}}$, respectively. Here, the reference timescale $T_{\mathrm{ref}} = L/U_{\infty}$, is equivalent to the time taken for the fluid to advect one wagon length (L) at the free-stream velocity (U_{∞}). The adherence to the Courant number restriction was checked after the simulations were completed. The non-iterative fractional-step method was employed to integrate the flow equations as the maximum cell Courant number remained below unity, noting that it is a requirement for stability of that time-integration scheme. The *Bounded Central Difference* scheme was used to treat the convection terms of the momentum equation, given the high Reynolds number involved. For time-advancement of the transient simulations, the *Bounded Second-Order Implicit* scheme was used.

Time-averaged results were obtained by averaging the flow once it was checked to have reached its asymptotic state by comparing statistics over different averaging time intervals. Note that the averaging time interval was increased with increasing gap size and yaw angle, due to the progressive reduction in the oscillation frequency with yaw. For zero yaw angle, the averaging time intervals for the smallest inter-wagon gap combination and the other gap sizes were $40T_{\mathrm{ref}}$ and at least $50T_{\mathrm{ref}}$, respectively, similar to the averaging time intervals used in Maleki et al. (2019). For non-yawed cases, as mentioned above, slightly higher averaging time intervals (at least $60T_{\mathrm{ref}}$) were used to increase the reliability of the (time-averaged) results. Note that no discernible changes were found in the drag and the time-averaged pressure distribution over the windward, top and leeward surfaces of the test wagon for averaging times of $60T_{\mathrm{ref}}$ and $120T_{\mathrm{ref}}$ for $G_{front} = 6.46W$ and $G_{base} = 0.3W$ at 20° yaw angle. As is discussed in Section. 3.4, the length of simulation for this gap size was greatly increased for yaw angles greater than 10° for analysing the side-force statistics. As a comparison, the averaging time interval used in IDDES simulations of a high-speed train conducted by Wang et al. (2018) was only 30 times the time taken for the fluid to travel along a single carriage of the train, i.e., equivalent to $30T_{ref}$.

2.5. Aerodynamic force coefficients

The relevant time-averaged aerodynamic force and moment coefficients are defined as follows:

$$C_D = \frac{F_x}{0.5\rho A_x U_{\infty}^2}, C_S = \frac{F_y}{0.5\rho A_y U_{\infty}^2}, C_{Mx,lee} = \frac{M_x}{0.5\rho A_y h U_{\infty}^2}, \quad (1)$$

where C_D and C_S are the drag and side force coefficients in the train's reference system, and $C_{Mx,lee}$ is the moment coefficient about the longitudinal axis that is calculated with respect to the bottom leeward side of the test wagon front face. In Eq. (1), U_{∞} is the freestream velocity, ρ is the density, h is the wagon height, A_x is a frontal area (width × height = 0.0784 m_2), A_y is a side area (length × height = 0.438 m_2), and M_x is the moment about the longitudinal axis.

In this study, the time-averaged pressure distribution at a surface is calculated in terms of the local pressure coefficient. This is defined as

$$C_p = \frac{P_t - P_{\mathrm{ref}}}{0.5\rho U_{\infty}^2}, \quad (2)$$

where P_t is the time-averaged static pressure, U_{∞} is the uniform wind speed, ρ is the density and P_{ref} is a suitable reference pressure, here taken at a centreline point on top surface of the wagon at $x = 0.75L$ to allow a better comparison with experimental results.

2.6. Proper orthogonal decomposition

In this section, a brief description of the principal of Proper orthogonal decomposition (POD) is given. For a detailed review of the derivation and implementation of POD, the reader is referred to Berkooz et al. (1993). The POD approach provides an energy efficient decomposition of the fluctuating part of a velocity field:

$$\vec{u}(\vec{x},t) = \vec{U}(\vec{x}) + \vec{u}'(\vec{x},t) = \vec{U}(\vec{x}) + \sum_{n=1}^{N} a_n(t)\vec{\varphi}_n(\vec{x}), \quad (3)$$

where U and u' denote the time-averaged and fluctuating components of the velocity field. The normalized base functions $\vec{\varphi}_n$ are spatially orthogonal, while the mode coefficients a_n are uncorrelated in time. In particular,

$$\langle \vec{\varphi}_i \cdot \vec{\varphi}_j \rangle = 1 \ \& \ \overline{a_i a_j} = \lambda_i (i=j), \quad (4)$$

$$\langle \vec{\varphi}_i \cdot \vec{\varphi}_j \rangle = 0 \ (i \neq j) = 0 \ (i \neq j), \quad (5)$$

where the overbar and angle brackets are indicative of temporal averaging and spatial integration, respectively. The eigenmodes of the two-point correlation matrix provides the POD modes $\vec{\varphi}_n$:

$$C\vec{\varphi}_n = \lambda_n \vec{\varphi}_n; \text{with} C_{ij} = \overline{\vec{u}'(\vec{x}_i,t) \cdot \vec{u}'(\vec{x}_j,t)}. \quad (6)$$

The eigenvalues, λ_n, indicates the contribution of the corresponding POD mode to the total fluctuating energy:

$$\langle \overline{\vec{u}'(\vec{x}_i,t) \cdot \vec{u}'(\vec{x}_i,t)} \rangle = \sum_{n=1}^{N} \lambda_n. \quad (7)$$

The most dominant modes can be revealed by sorting the POD modes according to decreasing eigenvalues. This approach has been widely used as one of the powerful methods to identify the dominant coherent flow structures. A subset of POD modes can be used to reconstruct a low-order representation of the variation of the sequence of fields, while individual modes or mode pairs can represent dominant persistent time-varying features. For time resolved data, as is the case here, for each mode, POD provides the time variation of the mode's contribution to the original time sequence.

2.7. Grid and timestep resolution

The mesh independence study presented here is for one representative gap combination $G_{front} = 0.3W$ and $G_{base} = 3.23W$ at $\psi = 0^{\circ}$ and $\psi = 10^{\circ}$. This gap combination was selected due to the availability of the wind-tunnel pressure measurements taken at 0° yaw angle. Note that the present study follows on from a more complete study on the influence of spatial and temporal resolution for the non-yawed case, see reference (Maleki et al., 2019). Hence, a more restricted resolution study was undertaken here. Predictions are reported for two grids, referred to as the *coarse* and *fine* grids.

For $G_{front} = 0.3W$ and $G_{base} = 3.23W$ at $\psi = 10^{\circ}$, the total number of cells for the coarse and fine grids were 2.8 and 17 million, respectively. The critical meshing parameters are listed in Table 3. The cell size was reduced (halved) and the corresponding number of inflation layers on the wall boundaries was increased between these two different meshes.

Fig. 3(a) and (b) show the locations of the centrelines around the test wagon where the pressure coefficient was recorded for comparison with experimental measurements. Note that the purple alignment (e-f-g-h) displayed in Fig. 3(b) is to show the variation in the pressure coefficient on the windward, top, leeward and base surfaces of the test wagon for the complete yaw angle range, presented later in Section. 3.3.1. As is displayed in Fig. 3(c), there is a good match between the C_p predictions from the coarse and fine meshes over the front and top surface, except immediately upstream of the trailing edge, where the coarse mesh over-predicts C_p by $\simeq 0.02$. Considering the small magnitude of pressure on the base surface, the difference between predictions for these two grids and the experimental variation is relatively minor over that region (in terms of the contribution to the drag). The drag predictions of the coarse and fine grids are 0.050 and 0.055, respectively. This suggests further grid refinement is likely to result in little change.

Fig. 3(d) shows a discernible change in the pressure fields between the coarse and fine grid over the front surface. The largest difference in C_p between the coarse and fine grid occurs near the windward edge of the front face, suggesting the grid resolution is insufficient over that region. Little difference in C_p can be observed between the two grids along both the windward and leeward surfaces. While a small difference in C_p is apparent between the two grids over the base face, the pressure magnitude is small. The slight difference between the fine and coarse grids indicates that only a small change would result from the use of a finer grid and smaller time-step. Hence, this grid resolution appears sufficient, and more expensive simulations based on a finer grid would not seem justified, especially in view of the large number of simulations required for this study.

3. Results and analysis

3.1. Time-averaged aerodynamic forces and moments

The IDDES predictions of the drag coefficient, C_D, the side force coefficient, C_S, and the moment coefficient, $C_{Mx.lee}$, for the various G_{front} and G_{base} combinations up to 20° yaw angle are presented in Fig. 4 (a)–(c). Additionally, the aerodynamic force coefficients for yaw angles of 30°, 45° and 90° for the two loading configurations, $G_{front} = 0.3W$ and $G_{front} = 6.46W$ at constant $G_{base} = 0.3W$, are shown in Fig. 4 (d)–(f).

As discussed in (Maleki et al., 2019), the highest drag experienced by a wagon with no cross-wind occurs where it is placed downstream of a large gap size, leaving space for the upstream shear layers to fully impinge on its front face, while the smallest drag occurs for the smallest inter-wagon gap combination. As expected, an increase of G_{front} causes the drag profile to be increased up to 20° yaw angle (See Fig. 4 (a)). For $G_{front} = 6.46W$, the drag profile continues to grow up to 30° yaw angle, where the C_D is increased by almost 2.23 times compared to its zero yaw angle, after which it slightly drops up to 45° yaw angle and then falls dramatically up to 90° yaw angle. For the smallest inter-wagon gap size at 90° yaw angle, the drag coefficient was found to be approximately zero, which it should be based on symmetry considerations. For $G_{front} = 6.46W$ at 90° yaw angle, the drag coefficient was recorded as 0.41. It is evident that the large upstream gap size of $6.46W$ allows the separating flow structures from the upstream wagon to travel inside the upstream gap, increasing the drag coefficient compared to that with a minimal gap ($G_{front} = 0.3W$).

An increase in G_{base} at constant $G_{front} = 0.3W$ slightly increases the C_D up to 20° yaw angle (see Fig. 4 (a)). For the smallest inter-wagon gap size,

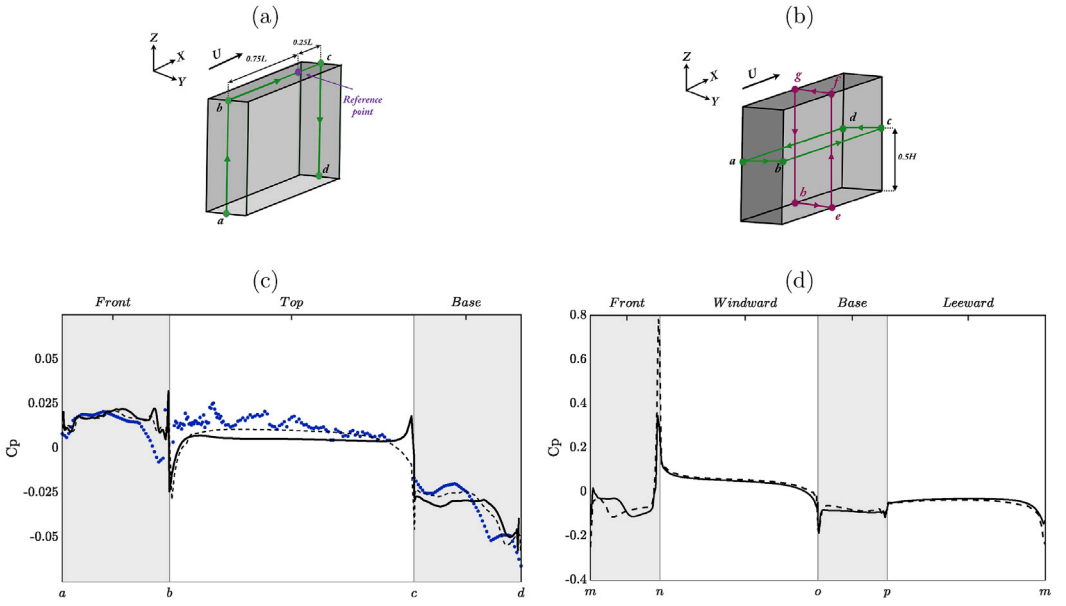

Fig. 3. (a) Coordinate system and the centrelines ($z = 0$) at 0° yaw angle used in the present study. (b) Coordinate system and the centrelines ($z/H = 0.5$) at 10° yaw angle used in the present study. (c) Mean surface pressure coefficient, C_p, of the multiple wagon setup at $G_{front} = 0.3W$ and $G_{base} = 3.23W$ at 0° yaw angle. (d) Mean surface pressure coefficient, C_p, of the multiple wagon setup at $G_{front} = 0.3W$ and $G_{base} = 3.23W$ at 10° yaw angle.

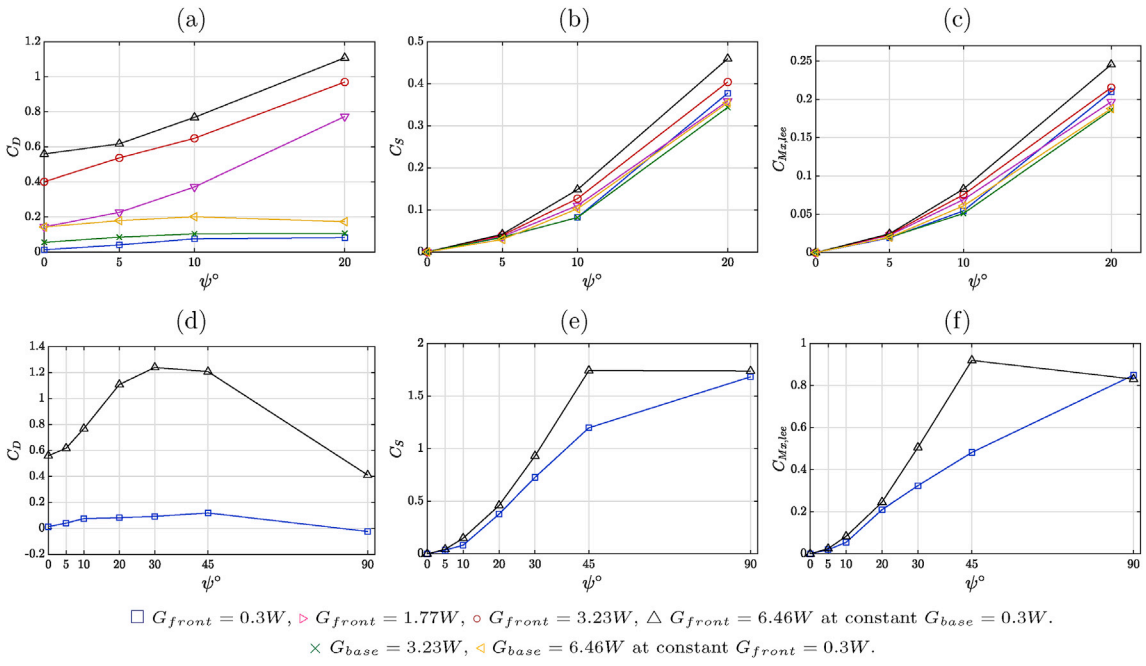

Fig. 4. Computational predictions of drag coefficient, C_D, side force coefficient, C_S, lee moment coefficient and $C_{Mx,lee}$ for the various G_{front} and G_{base} combinations with yaw angle.

the drag continues to increase from $\psi = 20°$ to $\psi = 45°$. It is evident that the rate of change of drag as G_{base} is increased is much smaller than caused by an increase in G_{front} at each yaw angle. This occurs as the front gap size remains the dominant influence on drag, while the primary contributor to the drag growth as G_{base} is increased is the reduction in the base pressure.

The influence of loading configuration on C_D up to 20° yaw angle can be clearly seen in Fig. 4 (a). For $\psi \leq 5°$, the highest rate of change of C_D between any of the two upstream gap sizes occurs over the upstream gap range $1.77W - 3.23W$, where C_D increases by approximately 2.75 and 2.4 times for 0° and 5° yaw angle, respectively. However, for $\psi \geq 10°$, the highest drag growth occurs over the gap size of $0.3W - 1.77W$. For 10° and 20° yaw angle, the drag penalty increases by approximately 5 and 9.5 times over this gap range, respectively. An increase of G_{front} from $3.23W$ to $6.46W$ only slightly increases the drag penalty for $\psi \geq 10°$ (by about 17%). These results indicate the strong benefits of maintaining an inter-wagon gap size below $1.77W$ consistent with previous non-yawed studies of Li et al. (2017) and Maleki et al. (2019).

Furthermore, the side force presented in Fig. 4(b) and (e) increases for all the loading configurations with increasing yaw angle. It can be seen in Fig. 4(b) that the rate of C_S growth as a function of yaw angle is greater than that caused by an increase in gap size, highlighting the fact that the dominant effect on an increase in C_S is the yaw angle, while the loading configuration is a secondary effect, as might be expected.

As displayed in Fig. 4(c and f), the moment coefficient $C_{Mx,lee}$ follows a similar trend to that of C_S, showing it progressively increases for all loading configurations with yaw. The highest value of $C_{Mx,lee}$ at each yaw angle occurs when the test wagon is located downstream of the largest gap size.

Perhaps closest to the present investigation is the experimental study of Giappino et al. (2018), in which the yaw angle of a model freight train, containing three wagons, was varied between 0° and 90°. The conclusions of both studies match each other qualitatively. For instance, they showed that both C_S and $C_{Mx,lee}$ increase rapidly up to approximately 50° yaw angle, after which they asymptotes to a constant value, consistent with the results presented here. However, it is difficult to make more than a semi-quantitative comparison due to a number of important differences between their experimental setup and that of the present study. In particular, they examined the single-stacked case. Other important differences were: lower number of upstream and downstream wagons in their experimental setup; the test wagon was downstream of the engine with a different rear shape; the presence of bogies in their experimental setup; their wagons (containers) appears to have had rounded edges, and differences in boundary layer thickness. Despite this, force coefficients are generally within a factor of two, where an appropriate comparison can be made. For instance, for 20° yaw, their side force coefficient was recorded as 1.1, while that for the current study was 1.8 (based on frontal area).

3.2. Time-averaged streamlines

This section aims to improve our understanding of how an increase in the upstream and downstream gap size with increasing yaw angle changes the flow topology around the test wagon, which in turn affects its drag. Thus, the predictions of time-averaged projected streamlines on a horizontal plane at $z/H = 0.5$ for $G_{front} = 1.77W$ and $3.23W$ at constant $G_{base} = 0.3W$, and $G_{front} = 6.46W$ and $G_{base} = 6.46W$ with yaw angle are presented in Figs. 5 and 6, respectively. Please note that the time-averaged streamlines for varying downstream gap sizes at the upstream gap size of $0.3W$ are similar to those of varying upstream gap sizes, and as such they have not been presented.

For $G_{front,base} = 0.3W$ at 0° yaw angle, it was shown in (Maleki et al., 2019) that the two counter-rotating vortices shield the gap and protect the front surface from impingement of upstream shear layers, leading to a low pressure over the entire face. However, with an increase of yaw angle, the greater area of the windward surface is exposed to the free-stream flow and the upstream wagon progressively shields a smaller area of the front surface. The free-stream entrainment from the windward to the leeward side only occurs through the top of the wagons, even at 20° yaw angle, due to the small gap size of $G_{front,base} = 0.3W$. The flow separation on the top surface of the wagons becomes progressively greater with yaw. This results in the progressive strengthening of the low pressure region on the top and leeward surface with increasing yaw angle. At 20° yaw angle, the low pressure region dominates over almost the entire leeward surface.

For $G_{front} = 1.77W$ at 0° yaw angle, the flow remains fully attached to the body of the downstream wagon as the length of the gap is shorter than the size of the time-averaged wake recirculation zone (Fig. 5). An

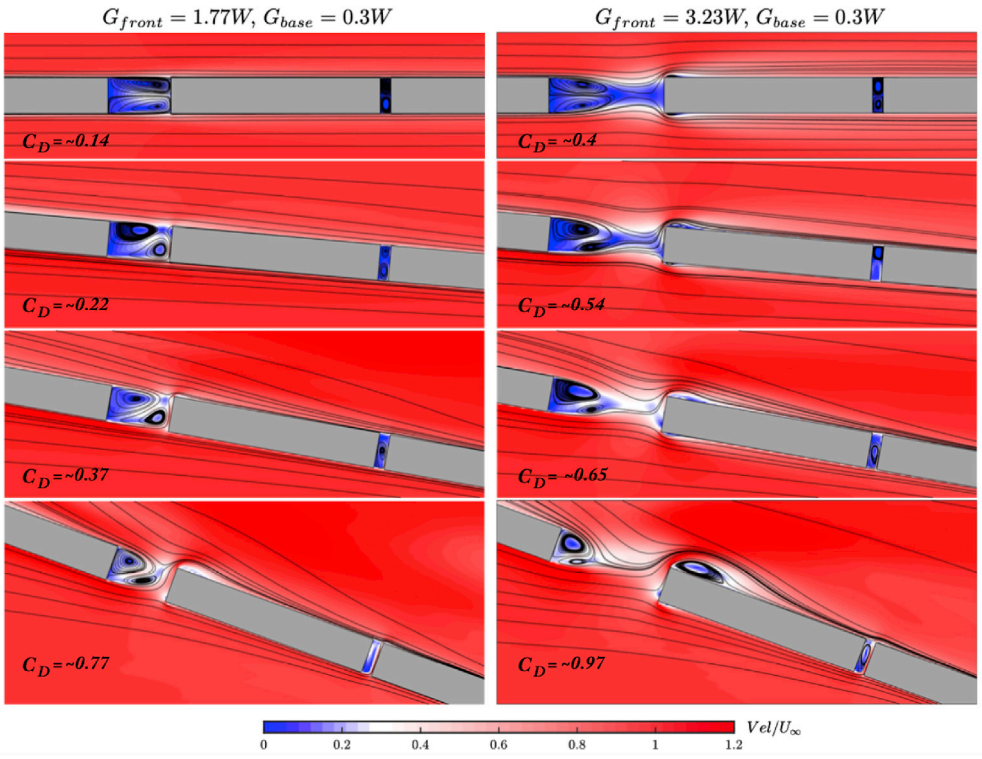

Fig. 5. Top-view of predicted time-averaged streamlines in the *x-y* plane at $z/H = 0.5$ for $G_{front} = 1.77W$ and $3.23W$ gap sizes at constant $G_{base} = 0.3W$ at yaw. The colours show the non-dimensional velocity (m/s). (For interpretation of the references to colour in this figure legend, the reader is referred to the Web version of this article.)

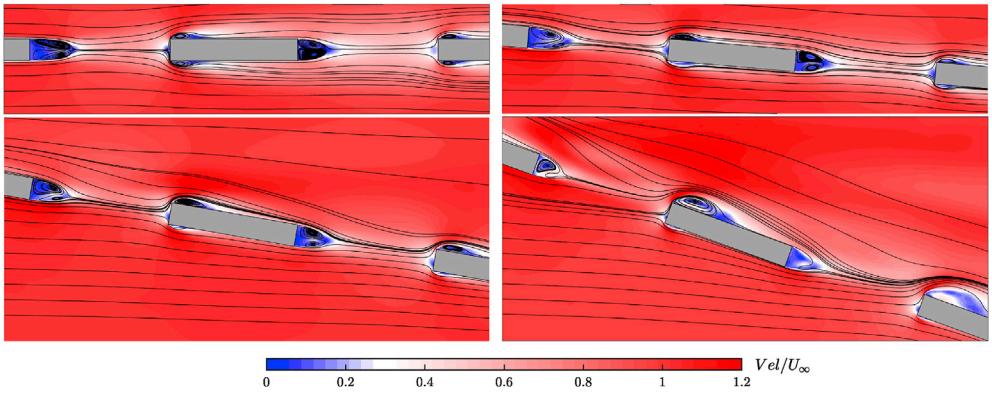

Fig. 6. Top-view of predicted time-averaged streamlines in the *x-y* plane at $z/H = 0.5$ for $G_{front} = 6.46W$ and $G_{base} = 6.46W$ with yaw. The colours show the non-dimensional velocity (m/s). (For interpretation of the references to colour in this figure legend, the reader is referred to the Web version of this article.)

increase of yaw angle to 5° causes no significant change to the flow topology, as the flow still remains attached to the body of the upstream wagon and the majority of the gap is still shielded from the free-stream entrainment. At 10° yaw angle, the flow separation along the leeward side of the upstream wagon becomes greater, while the flow becomes more attached along its windward surface. This causes the boundary-layer thickness at the leeward side to grow in size, increasing the size of vortex formed at that side, thus creating a more asymmetrical wake inside G_{front}. In addition to this, the larger area of the front and windward surface is being exposed to the free-stream flow. This once again results in the greater flow separation occurring on the top surface of the test wagon, lowering the pressure on the top and leeward surface, thus increasing the drag. At 20° yaw angle, the windward vortex no longer covers the gap, allowing the free-stream flow to impinge on almost half of the front surface, resulting into the sharp increase on C_p on the front face for $G_{front} = 1.77W$. This explains the underlying reason behind the high rate of change of drag occurring over the gap range $0.3W - 1.77W$ at 20° yaw angle shown in Fig. 4(a).

For $G_{front} = 3.23W$ at 0° yaw angle, the complete wake closure of the upstream wagon occurs, which in turn leaves space for the upstream side/top shear layers to travel inside the gap and impinge over the entire surface of the downstream face. It was shown in (Maleki et al., 2019) that the wake closure mechanism for gap size of $\geq 3.23W$ at 0° yaw angle is dominated by the inflow from the sides of the model. As yaw angle increases, once again, the level of wake asymmetry becomes greater. The flow impingement mechanism also changes from the upstream side shear layers to the free-stream flow, causing higher momentum to be transferred into the upstream gap. This creates the progressively larger flow separation on the top and leeward surface, which in turn reduces the pressure over these two regions with yaw.

No significant change in the mean streamlines can be observed as inter-wagon gap size increases from $G_{front} = 3.23W$ to $G_{front} = 6.46W$ with yaw (Fig. 6). Once again, the slightly larger drag for $G_{front} = 6.46W$ compared to $G_{front} = 3.23W$ for all the yaw angles tested here is induced by slightly higher momentum being transferred from the free-stream flow into the larger gap space, which in turn creates a much larger recirculation region at the leading edge of the test wagon leeward surface, thus slightly increasing the drag.

It is clear that an increase in G_{base} at constant $G_{front} = 0.3W$ causes no discernible change to the flow topology around the test wagon, except its wake. This means that the flow topology inside various G_{base} at constant $G_{front} = 0.3W$ is similar to that of their corresponding G_{front}, and as such the streamlines for $G_{base} = 3.23W$ and $6.46W$ at constant $G_{front} = 0.3W$ have not been presented. However, an increase in G_{front} causes the free-stream velocity inside G_{base} to be reduced, due to the unsteadiness of the oncoming flow. This lowers the momentum being entrained into that region (Fig. 6), and consequently the drag experienced on the wagon located downstream of the G_{base} becomes lower than that of the test wagon.

3.3. Pressure distribution

3.3.1. Time-averaged and standard deviation of pressure distribution

In this section, the variation in the mean pressure coefficient together with the standard deviation of the pressure coefficient on the windward, top, leeward and bottom surfaces of the test wagon are considered. The cases examine are: $G_{front} = 0.3W$, $1.77W$ and $6.46W$, for $\psi = 5^{\circ}$, 10° and 20°, as well as $G_{front} = 0.3W$ and $6.46W$ for $\psi \geq 30^{\circ}$. The predictions are presented in Figs. 7 and 8, respectively. Note that the surface pressure distribution for $G_{front} = 3.23W$ is similar to that of $G_{front} = 6.46W$ for $\psi = 10^{\circ}$ and 20°, and as such they have not been presented.

Additionally, note that the pressure distribution on these (four) surfaces for $G_{base} = 3.23W$ and $6.46W$ at constant $G_{front} = 0.3W$ have not been presented as: (i) the variation in G_{base} causes no significant change to the pressure distribution of the majority of these surfaces, except at their trailing edge where flow separation occurs; and (ii) $G_{base} = 3.23W$

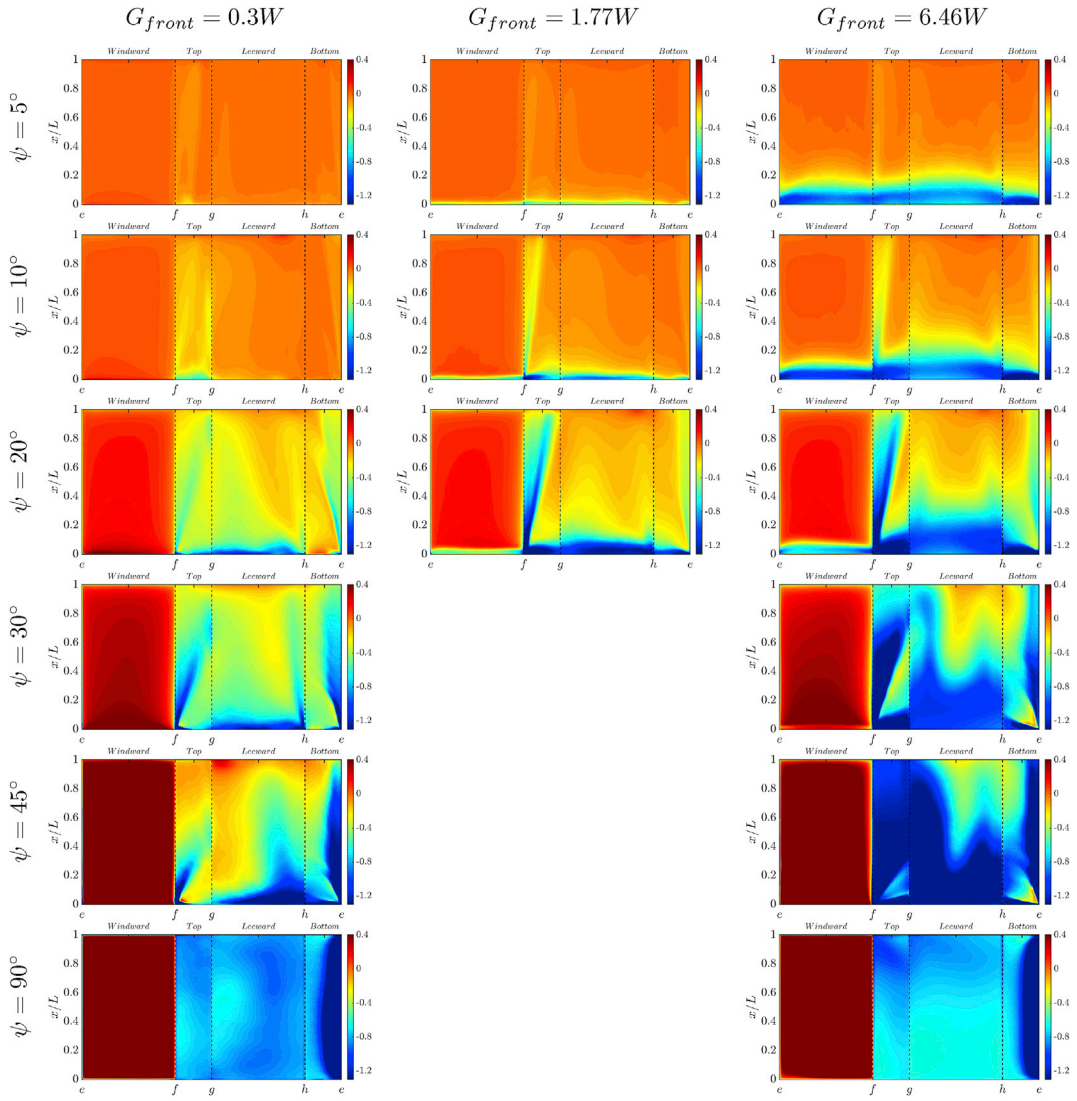

Fig. 7. Mean pressure coefficient on the windward, top, leeward and bottom surface of the test wagon subjected to $G_{front} = 0.3W$, $1.77W$ and $6.46W$ at constant $G_{base} = 0.3W$ with yaw angle.

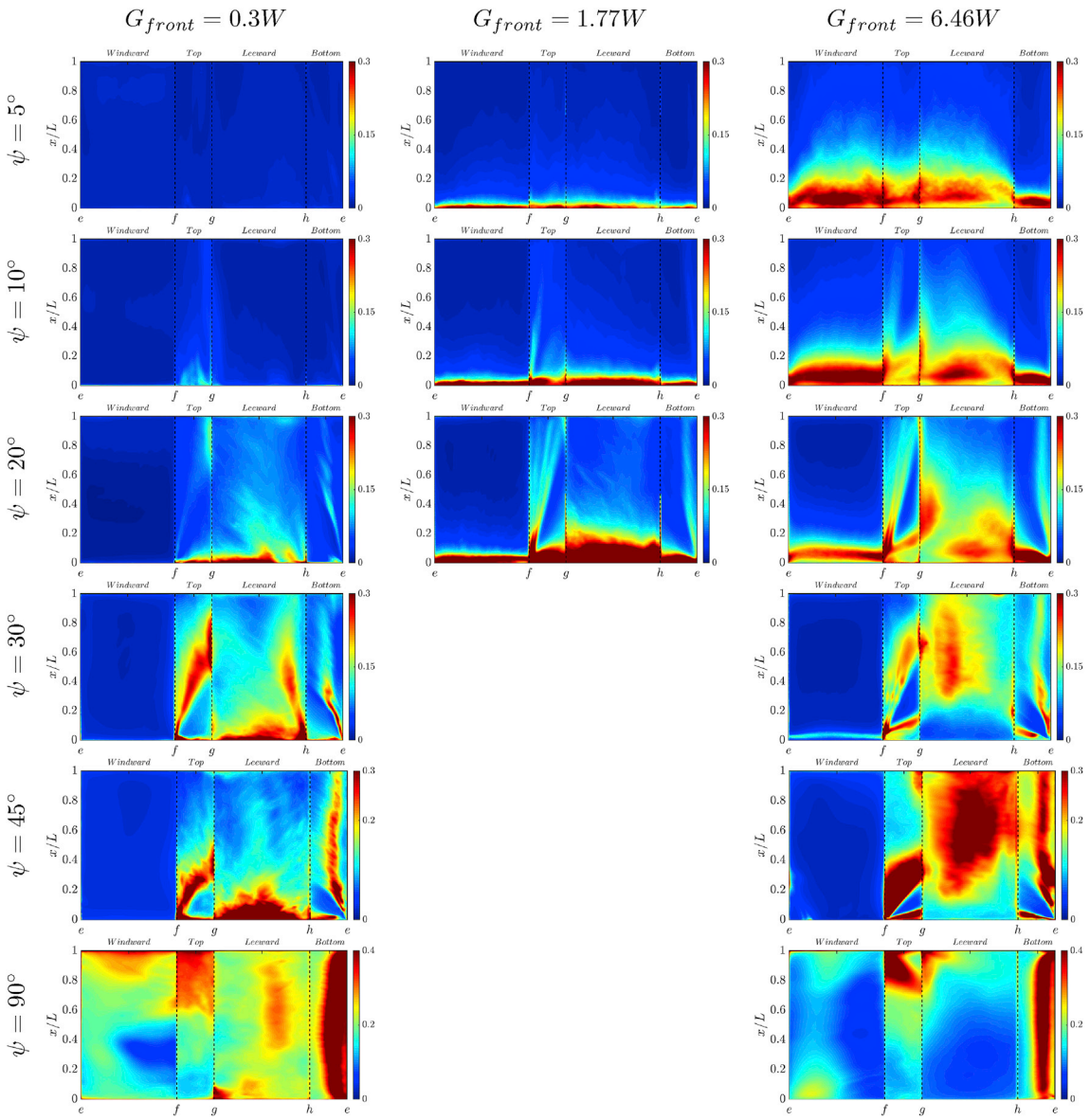

Fig. 8. Standard deviation of the pressure on the windward, top, leeward and bottom surface of the test wagon subjected to $G_{front} = 0.3W$, $1.77W$ and $6.46W$ at constant $G_{base} = 0.3W$ with yaw angle.

and $6.46W$ at a constant $G_{front} = 0.3W$ were not simulated for yaw angle greater than 20° in this study.

For $G_{front} = 0.3W$ and $G_{front} = 1.77W$ at $\psi = 5°$, an almost uniform pressure distribution can be seen on all the surfaces of the wagon. An increase of gap size to $G_{front} = 6.46W$ causes the slight asymmetrical flow separation to occur at the leading edge of all the surfaces.

An increase of yaw angle from 5° to 10° lowers the pressure over the roof and on the leeward surface for $G_{front} = 0.3W$, indicating the majority of the flow is still remained attached to the wagon for this gap size. However, an increase from $G_{front} = 0.3W$ to $G_{front} = 1.77W$ causes large flow separation to occur at the roof windward corner and the pressure on the leeward surface to be slightly lowered. Further gap enlargement to $G_{front} = 6.46W$ at $\psi = 10°$ results in larger flow separation at the leading-edge of all the surfaces with greater asymmetrical pressure distribution on the windward and leeward surface.

It can be seen that the mean pressure distribution undergoes no significant change as yaw angle is increased from 10° to 20°. The pressure distribution on the top and leeward surface is lowered and greater asymmetry in the pressure distribution can be seen on the windward and leeward surface for $G_{front} = 6.46W$ at $\psi = 20°$, increasing the size of recirculation region on the leeward side.

Further increase of yaw angle to 45° lowers the pressure on the top and leeward surface, consistent with an increase in the drag and side force with increasing yaw angle up to 45°, as shown in Fig. 4(d)–(e).

At $\psi = 90°$, the mean pressure distribution exhibits an uniform positive pressure on the windward surface and negative pressure distribution on all the other surfaces caused by the flow separation on the windward edge of the top surface.

Fig. 8 shows no region of high fluctuations in the surface pressure for $G_{front} = 0.3W$ up to $\psi = 10°$. However, a small region of high fluctuations starts to appear at the leading edge of the roof and the leeward surface at $\psi = 20°$, and appears to grow in size as yaw angle is increased up to 45°. The high level of unsteadiness over the roof for this gap size at $\psi = 30°$ and 45° is indicative of the unsteady longitudinal vortex development originating from the roof windward corner.

An increase of gap size from $G_{front} = 0.3W$ to $G_{front} = 1.77W$ only increases the region of high fluctuations over the roof and leeward surface. For yaw angles $\geq 10°$, once again, the longitudinal vortex starts to develop from the roof windward corner.

For $G_{front} = 6.46W$, with an increase of yaw angle, the region of high fluctuations on the windward side is reduced and almost disappears at $\psi = 30^{\circ}$ and 45°. The same trend of unsteadiness can be seen over the roof up to $\psi = 30^{\circ}$ for the largest gap size, while the region of high fluctuations is shortened and only extends up to almost half of the roof at $\psi = 45^{\circ}$. It can be seen that the time-averaged flow hides the two regions with the high fluctuations on the leeward surface at $\psi = 20^{\circ}$. These two fluctuating regions correspond to the longitudinal vortices originating at the top and bottom corner of the test wagon leeward side, which remain close to the body of the test wagon up to the middle of the test wagon. They however, move further away laterally from the wagon as they convect downstream, explaining why these fluctuating regions do not extend up to the trailing-edge of the leeward surface. Once again, only one region of high fluctuations is apparent on the leeward surface for $G_{front} = 6.46W$ at $\psi = 30^{\circ}$, and it grows in size as yaw angle is increased to 45°. This corresponds to the two longitudinal vortices covering the entire leeward surface. The region with the high level of unsteadiness is the area where these two longitudinal vortices interact with each other, resulting in high fluctuations. At $\psi = 90^{\circ}$, the level of unsteadiness is much smaller over the roof and leeward surface compared to the other yaw angles as the flow is separated at the roof windward corner and does not reattach onto the wagon.

It can therefore be concluded that the dominant flow structure over the roof is the longitudinal vortex formed at the windward edge of the roof for $G_{front} = 0.3W$ at $\psi = 30^{\circ}$ and 45° and for $G_{front} \geq 1.77W$ at $\psi = 10^{\circ}$ up to 45°. However, the dominant flow structures at the leeward side are the two longitudinal vortices originating at the top and bottom corner for $G_{front} \geq 3.23W$ at $\psi \geq 5^{\circ}$ up to 45°. The source and development of these longitudinal structures for $G_{front} = 6.46W$ are further discussed in Section. 3.5.

3.3.2. Proper Orthogonal Decomposition analysis of pressure distribution

In this section, the results of a Proper Orthogonal Decomposition (POD) analysis of the pressure coefficient data on the top and leeward surfaces of the test wagon are presented. This focuses on the case $G_{front} = 6.46W$ and $G_{base} = 0.3W$ at $\psi \geq 20^{\circ}$.

The energy content of pressure coefficient over these two surfaces for modes 1–10 at $\psi \geq 20^{\circ}$ is presented in Fig. 9. Approximately 19% and 12% of the energy is contained in the first two modes at $\psi = 20^{\circ}$ and 30°, respectively. This suggests the first two modes of these two yaw angles provide a reasonable picture of dominant physics and the higher-order modes are associated to the less-coherent smaller-scale structures. However, the energy contained in the first POD mode at $\psi = 45^{\circ}$ and 90° is significantly greater than that in the second mode, likely indicating they are unrelated to each other.

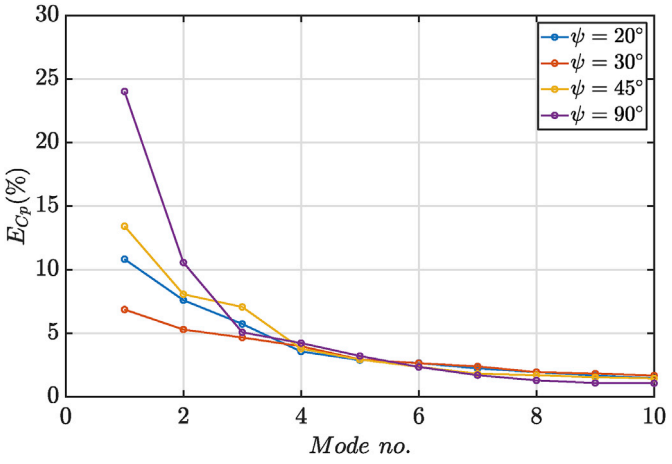

Fig. 9. Energy of the first 10 pressure coefficient POD modes on the top and leeward surfaces of the test wagon subjected to $G_{front} = 6.46W$ and $G_{base} = 0.3W$ at $\psi \geq 20^{\circ}$.

The first two POD modes at $\psi \geq 20^{\circ}$ are displayed in Fig. 10. In general, for 20° and 30° yaw angles, the form of mode 1 and 2 is quite similar to each other, noting that the main structures on these two surfaces for mode 2 take place further downstream compared to those of mode 1 and that the sign of its eigenvectors is reversed. This indicates a coupling between these two antisymmetric modes, suggesting the mode 1 and 2 might be a pair. However, at $\psi = 45^{\circ}$ and 90°, it is clear that the forms of mode 1 and 2 are different from each other, and therefore they are not a pair.

To further explore this and investigate the presence of periodicity in the flow on these two surfaces, the temporal information of the first two POD modes at $\psi = 20^{\circ}$ and 30° are displayed in Fig. 11. Please note that the variation in the temporal coefficients is shown based on full-scale equivalent time, which was defined in terms of the ratio of the full-scale to model-scale velocities and the geometric model scale. It is clear that these two coefficients for the two yaw angles are generally offset from each other by about 90°, suggesting that modes 1 and 2 are in fact a pair. Additionally, it can be seen that there are many instances where these two coefficients repeat clear patterns, suggesting there is an underlying periodicity in the flow.

The phase-average results on the top and the leeward surfaces of the test wagon for $\psi = 20^{\circ}$ are shown in Fig. 12 to visualise the presence of quasi-periodicity in the flow. Note that the phase-averaged results at $\psi = 30^{\circ}$ are not presented as the periodicity in the flow occurs at the small region of the leeward surface trailing-edge. The first two oscillating POD modes were used as the reference signal for binning the data into 16 bins (each bin is $\pi/8$ wide). The three most energetic modes (mode 0, 1 and 2) were then used for reconstructing the time-dependent behaviour. These results clearly show a periodic shortening and lengthening of the mean recirculation region formed at the leading-edge of leeward surface. However, the recirculation region on the top surface was found to be almost quasi-steady, as it undergoes no significant change and resembles the structure of the time-average flow shown in Fig. 7.

3.4. Analysis of side-force statistics

One of the major concerns to the freight industry is the stability of freight vehicles in cross-wind. To calculate the risk of freight vehicle overturning, one of the important pieces of information required to be gained is the variation of the aerodynamic side force coefficient with yaw angle. Hence, this section aims to provide information on the side force fluctuations that could be used for the vehicle overturning calculation.

In this section, only the loading configuration of $G_{front} = 6.46W$ and $G_{base} = 0.3W$ was selected to examine the extreme fluctuations in the side-force coefficient for a double-stacked wagon at $\psi \geq 10^{\circ}$. The primary reason behind this gap selection is that this load configuration is the most exposed case for varying G_{front}, thus experiencing the higher peak side-force coefficient than the smaller gap sizes. Additionally, it is computationally very expensive to obtain reliable statistics for all loading configurations in cross-wind.

An averaging time of 1 s was selected for calculating the peak side force coefficient. That time period is selected since the required time for a train to overturn during a wind gust is often stated to be around 1–3 s (Baker et al., 2004) and (Baker, 2010).

Fig. 13 shows the variation of the instantaneous side force coefficient based on full-scale equivalent time for a full-scale train. Note that the length of simulation for these particular cases was at least 6 times longer than the other loading configurations to increase the reliability of the statistics. Despite this, the length of simulation at $\psi = 90^{\circ}$ is evidently too short, and it would require a significantly longer sampling time to obtain reliable statistics due to much low frequency oscillations for this setup. It can be seen from the figure that a considerable number of peak events have a value higher than $\mu + 2\sigma$ for all the cases. However, all of them are short time events, so they do not strongly influence the 1 s running average.

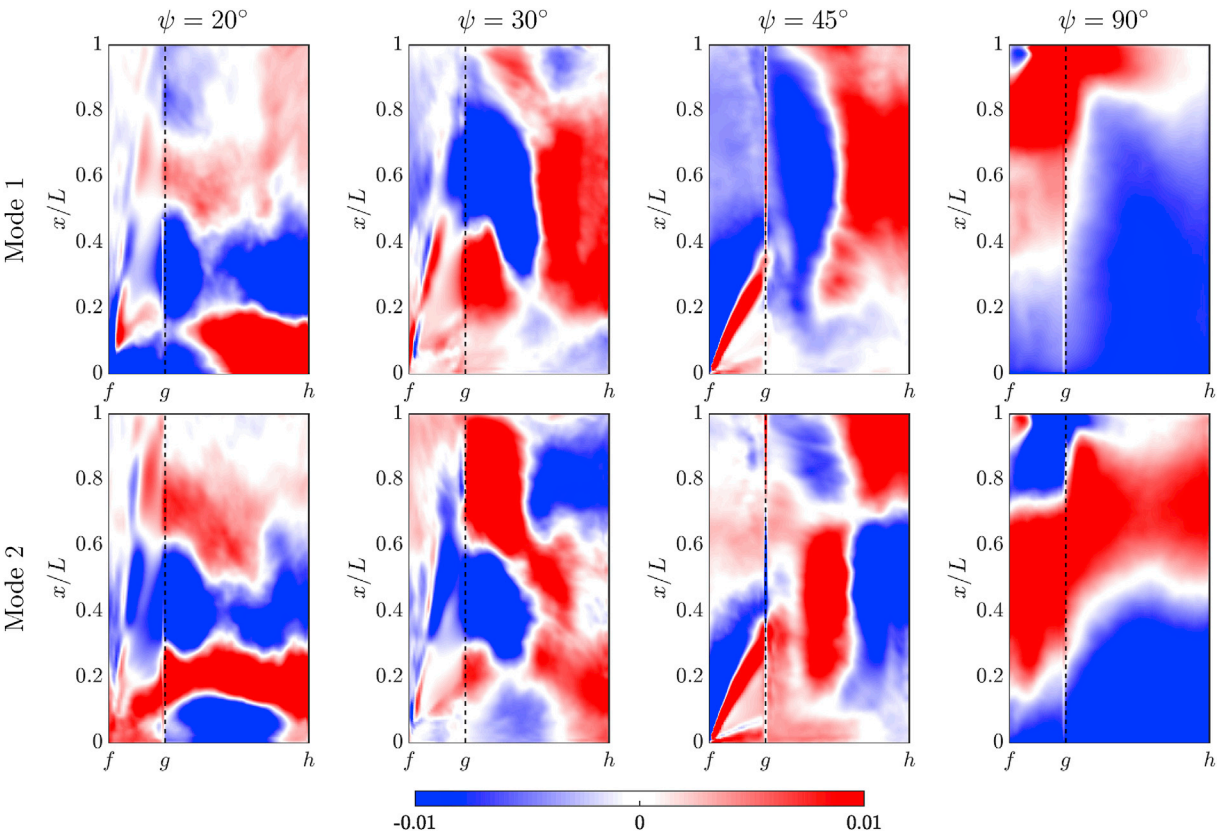

Fig. 10. Pressure coefficient POD mode 1 and 2 on the top and leeward surfaces of the test wagon subjected to $G_{front} = 6.46W$ and $G_{base} = 0.3W$ at $\psi = 20^{\circ}$ and 30°.

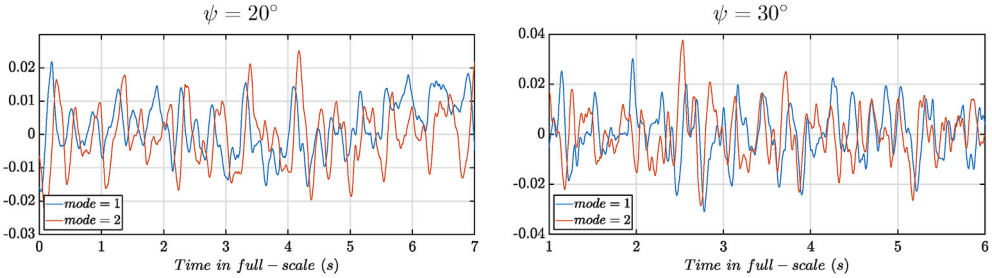

Fig. 11. Temporal coefficients of the first two POD modes of the pressure coefficient on the top and leeward surfaces of the test wagon subjected to $G_{front} = 6.46W$ and $G_{base} = 0.3W$ at $\psi = 20^{\circ}$ and 30°.

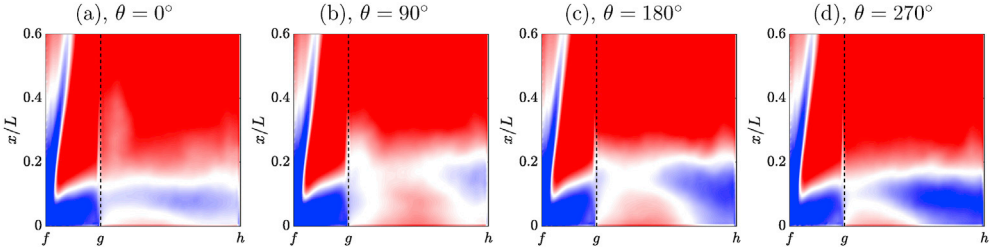

Fig. 12. Phase-averaged predictions of the pressure coefficient on the top and leeward surfaces of the test wagon subjected to $G_{front} = 6.46W$ and $G_{base} = 0.3W$ at $\psi = 20^{\circ}$, showing a periodic shortening and lengthening of the time-averaged recirculation region formed at the leading-edge of the leeward surface.

The probability distributions for C_s at $\psi \geq 10^{\circ}$ up to 45°, corresponding to the time series presented in Fig. 13, are displayed in Fig. 14. The vertical axis in Fig. 14 represents the probability of the relevant distribution, $P(i)$, multiplied by its standard deviation, $\sigma_p(i)$. The normal probability distribution with a corresponding similar variance is also presented in Fig. 14 for the reference. It is clear that the C_s probability distributions of these yaw angles do not display any obvious positive or negative skewness from a normal distribution, and show an approximately Gaussian behaviour. The slight difference between the C_s and the normal distribution in the right blue hand side tail of all the distributions,

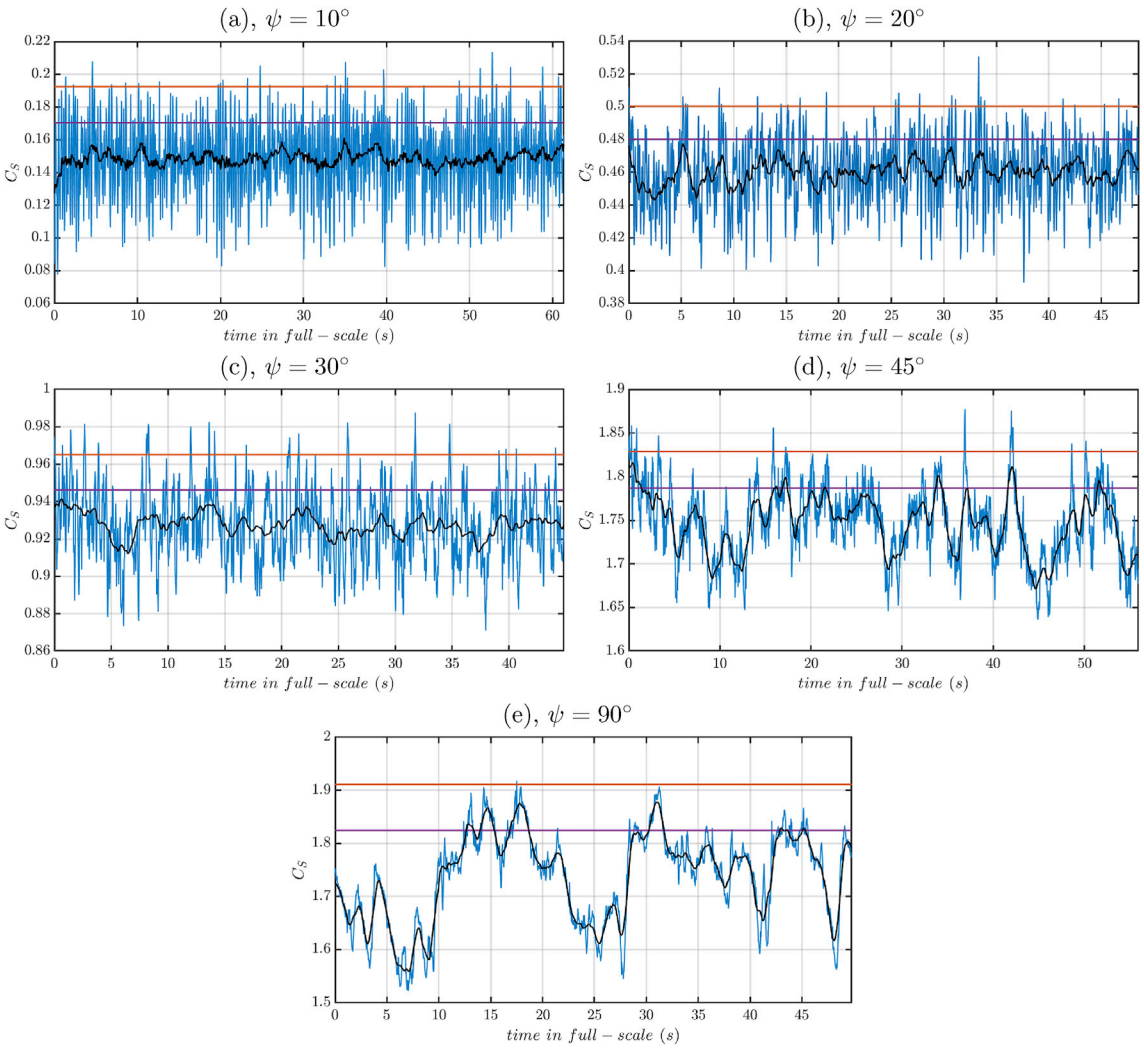

Fig. 13. vs time (full-scale) for $G_{front} = 6.46W$ and $G_{base} = 0.3W$ for yaw angle of $\geq 10^\circ$. Purple and orange lines represent the $\mu + \sigma$ and $\mu + 2\sigma$ for their corresponding yaw angle, respectively. (For interpretation of the references to colour in this figure legend, the reader is referred to the Web version of this article.)

except at $\psi = 30^\circ$, indicates the lower likelihood of occurrence of peak values compared to that of the normal distribution; however, this may be due to uncertainty introduced from a limited sampling time. This is in contrast to the experimental findings in Baker and Sterling (2009) where they found the non-Gaussian behaviour of the C_s for different yaw angles of a passenger train (see Fig. 21 in (Baker and Sterling, 2009)). The difference in the probability distribution between these two studies may possibly be explained by the geometrical differences between the passenger train with a rounded roof and containers with sharp edges investigated here.

The value of the peak side force coefficient, $\widehat{C_s}$, was calculated based on the maximum of the 1 s full scale equivalent averaged values of the side force. As shown in Fig. 15, the values of peak/mean C_s ratios remain between 1 and 1.09 for these four yaw angles, as the 1 s averaging time damps out the high frequency fluctuations. The ratio is at its maximum value at $\psi = 10^\circ$, around 1.09. It drops up to $\psi = 30^\circ$, where it reaches an almost unity, after which it increases to 1.05 at $\psi = 45^\circ$.

To analyse the values filtered by the 1 s running average, the pressure distributions associated with the extreme events at $\psi = 20^\circ$, 30° and 45° are displayed in Fig. 16. The ensemble average pressure distributions for the peaks events were calculated where the instantaneous C_s was greater or equal to the 96th percentile value (equivalent to $\mu + 2\sigma$). It is clear that the flow topology on all the surfaces, except the leeward surface, is very similar to the mean flow structure, shown in Fig. 7. This suggests an almost quasi-steady mean flow structure for the regions where the flow separation occurs on these surfaces. The size of the recirculation region over the leeward surface is slightly extended, and higher negative pressure can be observed at its trailing-edge for the three yaw angles. The peak surface-pressure at $\psi = 20^\circ$ is consistent with the phase-averaged result where the mean recirculation region has reached its longest length (See Fig. 11(d)).

3.5. Time-averaged longitudinal wake structure

To explore the downstream evolution of the time-averaged longitudinal vortical structures inside $G_{front} = 6.46W$ for yaw angles up to 45°, in-surface mean velocity vectors, the vortex structure boundaries and contours of streamwise vorticity (ω_x) in 5 planes parallel to the base surface of the model are presented in Fig. 17. Note that the longitudinal vortical structures at $\psi = 5^\circ$ are similar to those at $\psi = 10^\circ$, and as such they have not been presented. The location of these planes are also displayed in this figure.

For $G_{front} = 6.46W$ at zero yaw angle, no identifiable streamwise vortex was detected as the flow advects past the trailing edge corners. By $x/L = -0.8$, two pairs of time-mean counter-rotating streamwise vorticity concentrations appear downstream of the closure of the spanwise recirculation region formed at the back of the upstream wagon. These two vortex pairs grow in size as they convect downstream. The

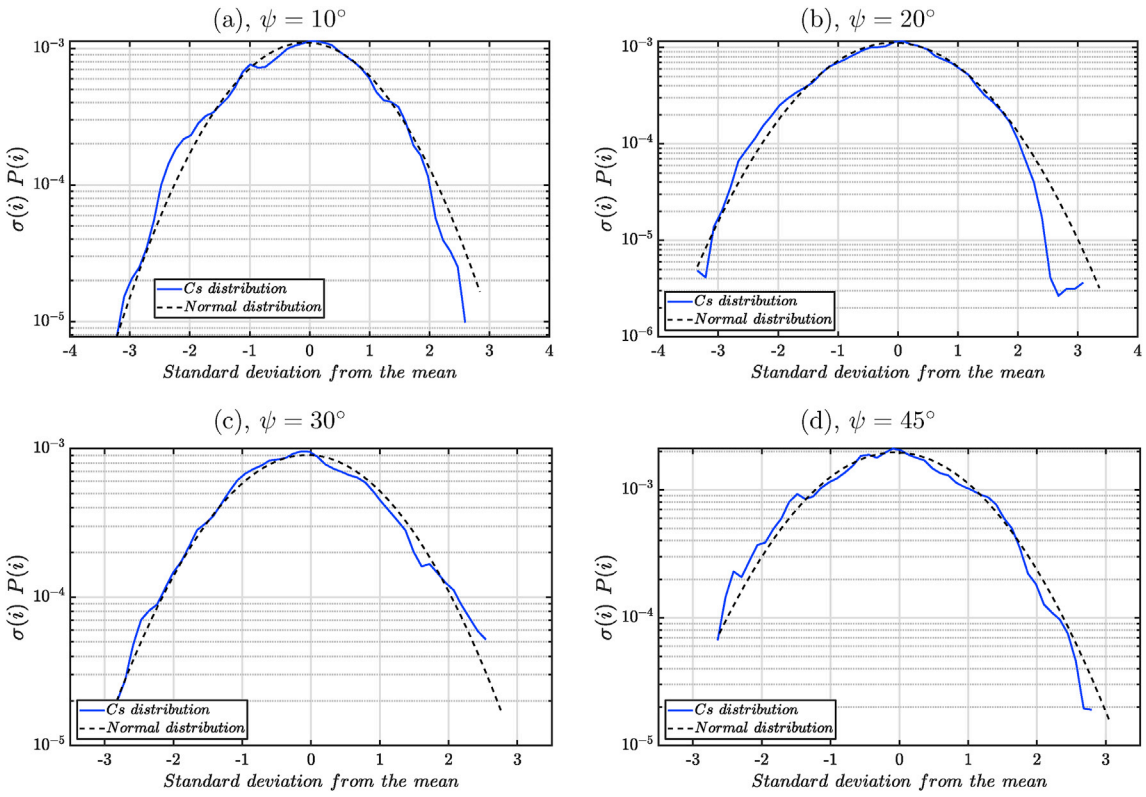

Fig. 14. Probability distribution of the side force coefficient for the time series data shown in Fig. 13 and the normal distribution with a corresponding similar variance.

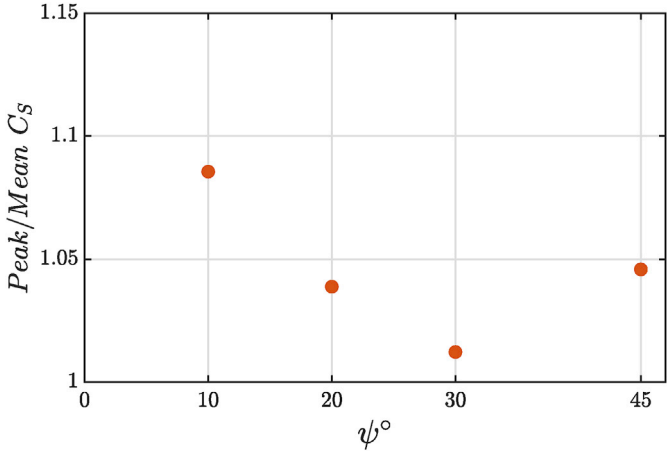

Fig. 15. Peak/mean side force coefficients ratios for $G_{front} = 6.46W$ and $G_{base} = 0.3W$ at $\psi = 10^\circ$, 20°, 30° and 45°.

source of these two vortex pairs may be the transverse entrainment of flow downstream of the wake, due to tilting and transport of the side boundary-layer vorticity into the wake. Following their impingement on the test wagon front face at $x/L = 0$, they become weaker, move outboard and continue to develop along the side surfaces of the downstream wagon ($x/L = 0.4$).

As yaw angle is increased, the downstream evolution of the mean longitudinal vortical structures undergoes a significant topology change. At 10° yaw angle, the two co-rotating negative streamwise vortices are formed near the trailing edge at $x/L = -1.2$, due to the flow separation from the roof of the upstream wagon. Additionally, a positive longitudinal vortex is created from the accelerated flow beneath the upstream wagon, rolling up over the leeward bottom corner. It is clear that these longitudinal vortices are the source of the longitudinal vortices developing inside the gap for yaw angles of $\geq 5^\circ$.

As the two co-rotating streamwise vortices convect downstream, they grow in size and move close to each other. By $x/L = -0.2$, they have moved so much towards the leeside inside the upstream gap that none of the longitudinal vortices impinge on the front face of the test wagon, in contrast to the zero yaw angle case. This in turn allows the free-stream to

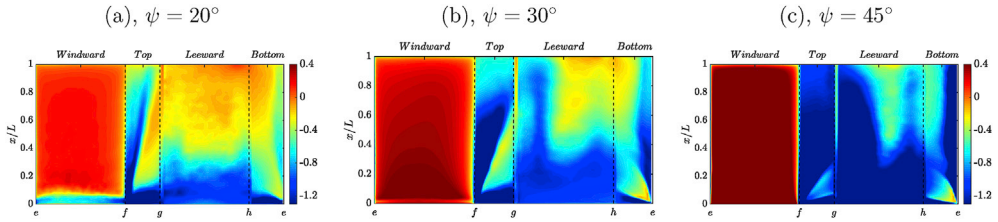

Fig. 16. Ensemble average pressure distribution corresponding to the peak side force event for $G_{front} = 6.46W$ and $G_{base} = 0.3W$ at $\psi = 20^\circ$, 30° and 45° shown in Fig. 13.

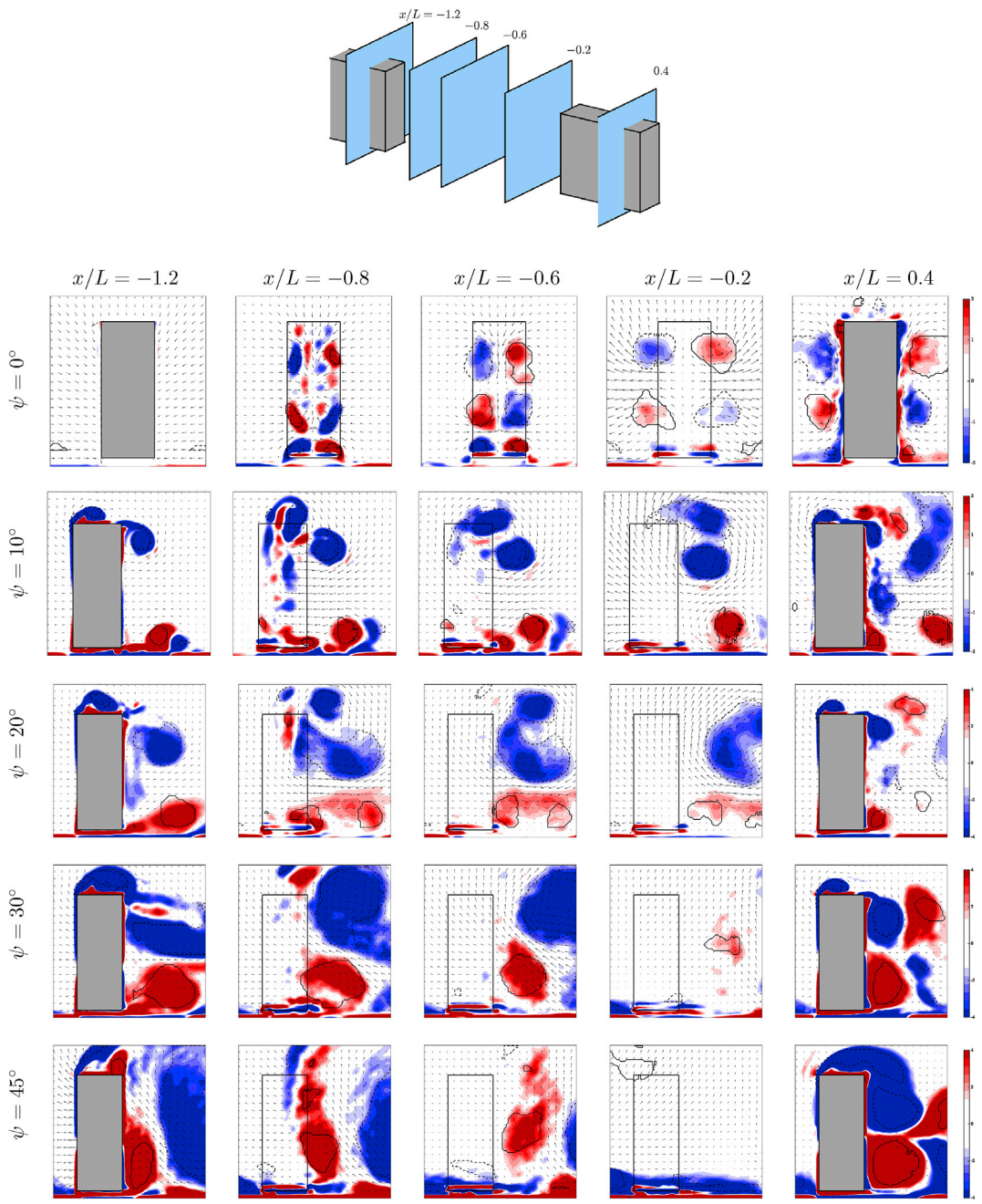

Fig. 17. The downstream evolution of vortical structures in the wake of the upstream wagon subjected to $G_f = 6.46W$ at $\psi \leq 45^{\circ}$. Filled contours are vorticity, ω_x. The vortex boundaries are identifier $\Gamma_2 = \pm 2/\pi$ and are black and solid for positive (counter-clockwise) rotation and blue and dashed for negative (clockwise) rotation. (For interpretation of the references to colour in this figure legend, the reader is referred to the Web version of this article.)

directly impinge on the downstream wagon front face. Following the free-stream impingement, once again, the negative and positive corner vortices start to develop over the roof and leeside ($x/L = 0.4$).

Further increase of yaw angle creates progressively larger and stronger corner vortices, particularly at the leeward top corner. The reason behind this is the location where they start to develop. The negative top leeward vortex has originated more upstream than other vortices, at inlet, and has traveled a much greater distance along the upstream wagon leeward surface, increasing its size and circulation. The downstream evolution of the wake for yaw angles of $\geq 20^{\circ}$ is similar to that of the 10° yaw angle, although the size and circulation (not presented here) of the longitudinal vortices for yaw angles of $\geq 20^{\circ}$ is much greater. In particular, following the free-stream impingement on the downstream wagon front face where they begin to develop over the roof and leeward surface.

Additionally, Fig. 18 displays the phase-averaged results of the longitudinal vorticity to verify the region of high fluctuations corresponds to the longitudinal vortices covering the entire leeward side of the test wagon, as discussed in Section. 3.3.1. The time-dependent behaviour was reconstructed using the two most energetic fluctuating POD modes (modes 1 and 2). This clearly shows the strong fluctuations in the vorticity field at the half-height of the loaded wagon that are well-correlated with the pressure fluctuations seen in Fig. 8.

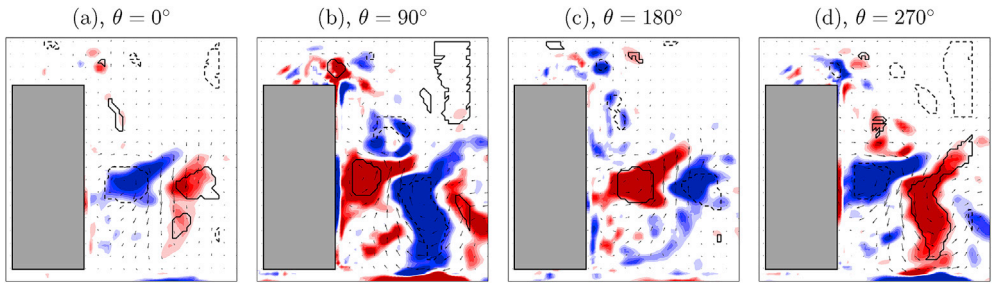

Fig. 18. Phase-averaged predictions of the fluctuating longitudinal vorticity, ω_x, at $x/L = 0.4$ for $G_{front} = 6.46W$ at $\psi = 45°$ yaw angle.

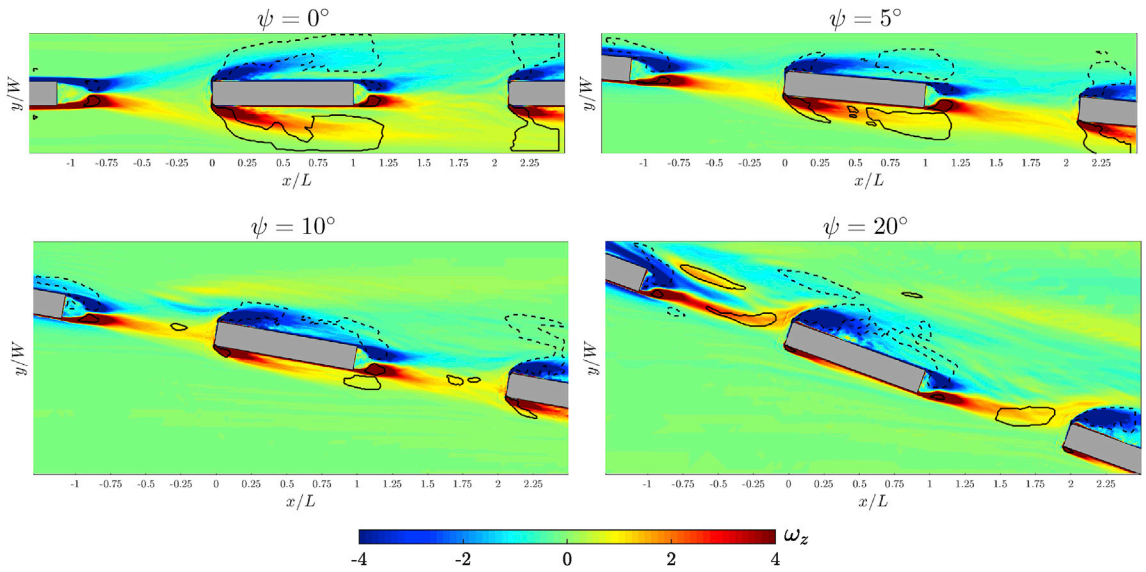

Fig. 19. Time-averaged predictions of the upstream wagon and the test wagon wake for $G_{front} = 6.46W$ and $G_{base} = 6.46$ at $\psi \leq 20°$.

3.6. Time-averaged vertical vorticity

The time-averaged wake structure in the middle horizontal plane ($z/H = 0.5$) is depicted in Fig. 19 by colour contours of vertical vorticity (ω_z) overlaid with boundaries denoting the vortex structures for $G_{front} = 6.46W$ and $G_{base} = 6.46$ at $\psi \leq 20°$.

At 0° yaw angle, the symmetrical development of the boundary layers with equal circulation in the separating shear layers from the sides of the train results in the formation of a time-mean symmetric pair of counter-rotating vortices in the near wake of the upstream wagon and the test wagon.

With an increase of yaw angle, boundary-layer separation is accentuated from the leeward side edge and progressively reduced or eliminated at the windward leading edge. On the leeward side, the separating shear layer forms a stronger more coherent vortical structure that leads to a thicker and weaker boundary layer separating from the trailing edge. Thus, for higher yaw, the separating shear layer from the windward trailing edge dominates the near- and intermediate-wake flow. Indeed this results in this shear layer impinging onto the downstream wagon front face and significantly alters the mean oncoming flow experienced by that wagon.

Overall, the flow structure inside the base gap ($G_{base} = 6.46W$) is very similar to that inside the front gap ($G_{front} = 6.46W$) at various yaw angles, as might be expected.

4. Conclusion

The drag coefficient of a double-stacked test wagon subjected to different upstream (G_{front}) and downstream (G_{base}) gaps under cross-wind conditions was predicted using Improved Delayed Detached Eddy Simulations. These results can be applied to approximately estimate and potentially improve fuel economy of freight trains. It is shown that the highest rate of change of C_D occurs in the upstream gap size range $1.77W - 3.23W$ (W = wagon width) for yaw angles $\leq 5°$, and $0.3W - 1.77W$ for yaw angles $\geq 10°$. Here, $G = 0.3W$ is the standard interwagon gap and $G = 6.46W$ corresponds to the gap associated with an unloaded wagon. This highlights the importance on maintaining small upstream gaps between loaded containers, with the benefit increasing for increased yaw. The rate of change of drag was much greater on increasing the upstream gap rather than the downstream gap at each yaw angle.

Additionally, the side force and moment coefficients as a function of loading configuration and yaw angle were predicted and analysed in view of the risks associated with freight vehicles overturning under strong cross-winds.

The probability distribution of the side force coefficient was calculated for the loading configuration of $G_{front} = 6.46W$ and $G_{base} = 0.3W$ for yaw angles $\geq 10°$. They exhibited an approximately Normal distribution without any strong indication of skewness or kurtosis, although this may be due to inadequate sampling times as there was some indication of non-normal characteristics for a passenger train carriage reported by Baker and Sterling (2009).

For $G_{front} = 0.3W$ at yaw angles of 30° and 45°, and $G_{front} = 1.77W$ at yaw angles of $\geq 10°$ up to 45°, the dominant flow feature around the test wagon is the unsteadiness in the flow over the roof associated with an unsteady longitudinal vortex originating at the windward corner of the roof. For $G_{front} \geq 3.23W$ at yaw angles of $\geq 5°$ up to 45°, in addition to the roof vortex, the flow structure at the leeward side is dominated by two longitudinal vortices originating from the top and bottom corners. They

are formed at the leading-edge of the leeward surface and remain attached to the body of wagon to approximately the middle of the wagon, before then moving further away laterally from the wagon.

A POD analysis was performed of the surface pressure on the top and side surfaces of the test wagon for $G_{front} = 6.46W$ and $G_{base} = 0.3W$ for yaw angles $\geq 20^{\circ}$. A coupling was found between the two first antisymmetric modes at 20° and 30° yaw angles. The phase-averaged results at 20° yaw angle showed an almost quasi-steady state for the flow separation on the top surface as it resembles its corresponding mean flow structure. However, this analysis revealed a periodic shortening and lengthening of the time-averaged recirculation region formed at the leading-edge of the leeward surface.

CRediT authorship contribution statement

Siavash Maleki: Writing - original draft, Conceptualization, Methodology, Software, Investigation, Visualization, Data curation, Writing - original draft. **David Burton:** Conceptualization, Supervision, Project administration, Writing - review & editing. **Mark C. Thompson:** Conceptualization, Methodology, Supervision, Writing - review & editing, Funding acquisition, Project administration.

Declaration of competing interest

The authors declare that they have no known competing financial interests or personal relationships that could have appeared to influence the work reported in this paper.

Acknowledgement

The research described in this paper was supported by Pacific National Rail and an Australian Research Council Linkage Project Grant LP13100953. SM would also like to acknowledge partial PhD scholarship funding through this grant. The authors also acknowledge a generous computing time allocation from the National Computational Infrastructure (NCI) and Pawsey Supercomputer Centre (merit grants n67 and d71), supported by resources provided by the Pawsey Supercomputing Centre with funding from the Australian Government and the Government of Western Australia.

References

Ahmed, S., 1983. Influence of base slant on the wake structure and drag of road vehicles. ASME J. Fluids Eng. 105 (4), 429–434.
Baker, C.J., 2010. The simulation of unsteady aerodynamic cross wind forces on trains. J. Wind Eng. Ind. Aerod. 98 (2), 88–99.
Baker, C.J., Sterling, M., 2009. Aerodynamic forces on multiple unit trains in cross winds. J. Fluid Eng. 131 (10), 101103.
Baker, C.J., Jones, J., Lopez-Calleja, F., Munday, J., 2004. Measurements of the cross wind forces on trains. J. Wind Eng. Ind. Aerod. 92 (7–8), 547–563.
Berkooz, G., Holmes, P., Lumley, J., 1993. The Proper Orthogonal Decomposition in the analysis of turbulent flows. Annu. Rev. Fluid Mech. 25 (1), 539–575.
Engdahl, R., Gielow, R.L., Paul, J.C., 1986a. Train resistance-aerodynamics.: volume i of ii. intermodal car application. In: Railroad Energy Technology Conference II, 1987.
Engdahl, R., Gielow, R.L., Paul, J.C., 1986b. Train resistance-aerodynamics.: volume ii of ii. open top car application. In: Railroad Energy Technology Conference II, 1987.
European Rail Agency, 2008. Technical Specification for Interoperability (TSI 232/2008) - Rolling Stock Subsystem. EC, 96/48.
Flynn, D., Hemida, H., Soper, D., Baker, C., 2014. Detached-Eddy Simulation of the slipstream of an operational freight train. J. Wind Eng. Ind. Aerod. 132 (1–12).
Flynn, D., Hemida, H., Baker, C., 2016. On the effect of crosswinds on the slipstream of a freight train and associated effects. J. Wind Eng. Ind. Aerod. 156, 14–28.
García, J., Muñoz-Paniagua, J., Jiménez, A., Migoya, E., Crespo, A., 2015. Numerical study of the influence of synthetic turbulent inflow conditions on the aerodynamics of a train. J. Fluid Struct. 56, 134–151.
Giappino, S., Melzi, S., Tomasini, G., 2018. High-speed freight trains for intermodal transportation: wind tunnel study on the aerodynamic coefficients of container wagons. J. Wind Eng. Ind. Aerod. 175, 111–119.
Gielow, M.A., Furlong, C.F., 1988. Results of Wind Tunnel and Full-Scale Tests Conducted from 1983 to 1987 in Support of the Association of American Railroads' Train Energy Program. Technical Report.
Golovanevskiy, V.A., Chmovzh, V.V., Girka, Y.V., 2012. On the optimal model configuration for aerodynamic modeling of open cargo railway train. J. Wind Eng. Ind. Aerod. 107, 131–139.
Li, C., Burton, D., Kost, M., Sheridan, J., Thompson, M.C., 2017. Flow topology of a container train wagon subjected to varying local loading configurations. J. Wind Eng. Ind. Aerod. 169, 12–29.
Maleki, S., Burton, D., Thompson, M.C., 2019. Flow structure between freight train containers with implications for aerodynamic drag. J. Wind Eng. Ind. Aerod. 188, 194–206.
Mathey, F., Cokljat, D., Bertoglio, J.P., Sergent, E., 2006. Specification of LES inlet boundary condition using vortex method. Prog. Comput. Fluid Dynam. Int. J. 6, 58–67.
Raghunathan, R.S., Kim, H.D., Setoguchi, T., 2002. Aerodynamics of high-speed railway train. Prog. Aero. Sci. 38 (6–7), 469–514.
Raib, 2008. Detachment of Containers from Freight Wagons Near Cheddington and Hardendal, 1 March. Report 12/2009; 2009.
Shur, M.L., Spalart, P.R., Strelets, M. Kh, Travin, A.K., 2008. A hybrid RANS-LES approach with delayed-DES and wall-modelled LES capabilities. Int. J. Heat Fluid Flow 29 (6), 1638–1649.
Soper, D., Baker, C., Sterling, M., 2015. An experimental investigation to assess the influence of container loading configuration on the effects of a crosswind on a container freight train. J. Wind Eng. Ind. Aerod. 145, 304–317.
Spalart, P.R., 2009. Detached-eddy simulation. Annu. Rev. Fluid Mech. 41, 181–202.
Spalart, P.R., Jou, W., Strelets, M., Allmaras, S.R., 1997. Comments on the feasibility of LES for wings, and on a hybrid RANS/LES approach. Greyden Press, Columbus, pp. 137–147.
Wang, S., Burton, D., Herbst, A.H., Sheridan, J., Thompson, M.C., 2018. The effect of the ground condition on high-speed train slipstream. J. Wind Eng. Ind. Aerod. 172, 230–243.
Watkins, S., Saunders, J.W., Kumar, H., 1992. Aerodynamic drag reduction of goods trains. J. Wind Eng. Ind. Aerod. 40 (2), 147–178.